Assimilation of a coordinated fleet of uncrewed aircraft system observations in complex terrain: Observing System Experiments

Anders A. Jensen[a] James O. Pinto,[a] Sean C. C. Bailey,[b] Ryan A. Sobash,[a] Glen Romine,[a] Gijs de Boer,[c d e] Adam L. Houston,[f] Suzanne W. Smith,[b] Dale A. Lawrence,[g] Cory Dixon,[g] Julie K. Lundquist,[g h] Jamey D. Jacob,[i] Jack Elston,[j] Sean Waugh,[k] David Brus,[l] and Matthias Steiner[a]

[a] *National Center for Atmospheric Research, Boulder, Colorado*

[b] *University of Kentucky, Lexington, Kentucky*

[c] *Cooperative Institute for Research in Environmental Sciences at the University of Colorado Boulder, Boulder, Colorado*

[d] *NOAA Physical Sciences Laboratory, Boulder, Colorado*

[e] *Integrated Remote and In Situ Sensing, University of Colorado, Boulder, Colorado*

[f] *University of Nebraska-Lincoln, Lincoln, Nebraska*

[g] *University of Colorado, Boulder, Colorado*

[h] *National Renewable Energy Laboratory, Golden, Colorado*

[i] *Oklahoma State University, Stillwater, Oklahoma*

[j] *Black Swift Technologies, Boulder, Colorado*

[k] *National Severe Storms Laboratory, Norman, Oklahoma*

[l] *Finnish Meteorological Institute, Helsinki, Finland*

Corresponding author: James O. Pinto, pinto@ucar.edu

Early Online Release: This preliminary version has been accepted for publication in *Monthly Weather Review* cited, and has been assigned DOI 10.1175/MWR-D-22-0090.1.The final typeset copyedited article will replace the EOR at the above DOI when it is published.

ABSTRACT: Uncrewed aircraft system (UAS) observations from the Lower Atmospheric Profiling Studies at Elevation – a Remotely-operated Aircraft Team Experiment (LAPSE-RATE) field campaign were assimilated into a high-resolution configuration of the Weather Research and Forecasting (WRF) model. The impact of assimilating targeted UAS observations in addition to surface observations was compared to that obtained when assimilating surface observations alone using observing system experiments (OSEs) for a terrain-driven flow case and a convection initiation (CI) case observed within Colorado's San Luis Valley (SLV). The assimilation of UAS observations in addition to surface observations results in a clear increase in skill for both flow regimes over that obtained when assimilating surface observations alone. For the terrain-driven flow case, the UAS observations improved the representation of thermal stratification across the northern SLV which produced stronger upvalley flow over the eastern half of the SLV that better matched the observations. For the CI case, the UAS observations improved the representation of the pre-convective environment by reducing dry biases across the SLV and over the surrounding terrain. This led to earlier CI and more organized convection over the foothills that spilled outflows into the SLV, ultimately helping to increase low-level convergence and CI there. In addition, the importance of UAS capturing an outflow that originated over the Sangre de Cristo Mountains and triggered CI is discussed. These outflows and subsequent CI were not well-captured in the simulation that assimilated surface observations alone. Observations obtained with a fleet of UAS are shown to notably improve high-resolution analyses and short-term predictions of two very different mesogamma-scale weather events.

Accepted for publication in *Monthly Weather Review*. DOI 10.1175/MWR-D-22-0090.1.

1. Introduction

With the rapid increase in the commercial use of uncrewed aircraft systems (UAS) and recent advancements in the accuracy and reliability of UAS weather-sensing technologies, an abundance of UAS-based lower-atmospheric observations are expected to become available in the next 5 – 10 years. These observations are already being used to improve our understanding of the planetary boundary layer (PBL) (e.g., Luce et al. 2019) and to evaluate Numerical Weather Prediction (NWP) models (Cassano 2014; Witte et al. 2017; Moore 2018). Ongoing research has also demonstrated the potential value of targeted UAS observations to improve short-term weather forecasting by providing meteorologists with more timely observations where they are needed most (Koch et al. 2018) and to increase the accuracy of analyses used to initialize mesoscale prediction models (Jensen et al. 2021).

In the near future, a combination of dedicated atmosphere-sampling UAS (Chilson et al. 2019), commercial UAS with relevant atmospheric sensors, and targeted UAS measurements collected in areas of forecast uncertainty (e.g., Limpert and Houston 2018) could serve as key inputs for high-resolution, rapidly updating data assimilation (DA) systems. The role of commercial UAS in collecting observations for assimilation into NWP models is unclear, but the commercial airline analog indicates the potential of this new data stream (James and Benjamin 2017; Petersen 2016; Petersen et al. 2016), especially since these small UAS will primarily be flown in the lower atmosphere where in situ observations are currently sparse.

Regional observing system experiments (OSEs) are often used to ascertain the relative skill attributable to individual observational datasets as compared to typically assimilated datasets (Houtekamer and Zhang 2016). A limited number of OSEs have been performed to evaluate the relative impact of small UAS observations on the skill of analyses and short-term predictions produced with mesoscale modeling systems. Flagg et al. (2018) performed OSE studies using 3D variational (3DVAR) DA and demonstrated that UAS observations reduced biases and errors in predictions of boundary layer characteristics over open water. They noted the importance of optimizing the decorrelation length scale and recommended conducting more systematic studies to determine the scales over which UAS data should be spread. Leuenberger et al. (2020) indicate the potential value of assimilating UAS observations using an ensemble-based DA technique but provide limited details on the DA system and performance metrics.

In this study, the work of Jensen et al. (2021) is extended by performing a systematic evaluation of the impact of UAS observations on the simulation of mesogamma-scale flows. OSEs are performed to quantify the impact of assimilating UAS observations on the skill of mesoscale analyses and predictions for two disparate cases. A description of the two cases — terrain-driven flow reversal and convection initiation within a high alpine valley — and observational datasets used in this study are given in Section 2. The DA system configuration is briefly summarized in Section 3. Results of the OSEs including an assessment of both the analyses and free forecasts are given in Sections 4 and 5, respectively. In these sections, physical reasoning for the differences that were found is provided. Section 6 provides a summary and further discussion.

2. Case summaries and observations

Observational data used in this study were collected during the International Society for Atmospheric Research using Remotely-piloted Aircraft (ISARRA) Lower Atmospheric Process Studies at Elevation – a Remotely-piloted Aircraft Team Experiment (LAPSE-RATE) deployment (de Boer et al. 2020e). The field experiment occurred in Colorado's San Luis Valley (SLV, Fig. 1) in July 2018 with observations collected by a suite of UAS platforms, surface-based towers, surface-based mobile platforms and remote sensors whose data are largely available to the general scientific community (de Boer et al. 2020d). UAS were deployed across the northern half of the SLV each day and positioned to target a specific flow regime or process. UAS observations collected on 15 July 2018 targeted the pre-convective environment to help better simulate convection initiation (CI) while UAS observations collected on 19 July 2018 targeted sampling conditions relevant for predicting the reversal of terrain-driven flows.

The UAS deployment locations are shown in Figure 1 for both cases with details of the UAS platforms given in Table 1 and 2. Additional ground-based surface stations, sounding systems and remote sensors were also strategically deployed across the SLV as shown and Figure 1 and detailed in Tables 1 and 2.

a. Convection initiation case

On 15 July 2018, convective storms initiated within the SLV along outflow boundaries that formed in the surrounding higher terrain. Thunderstorm development was aided by mid-level

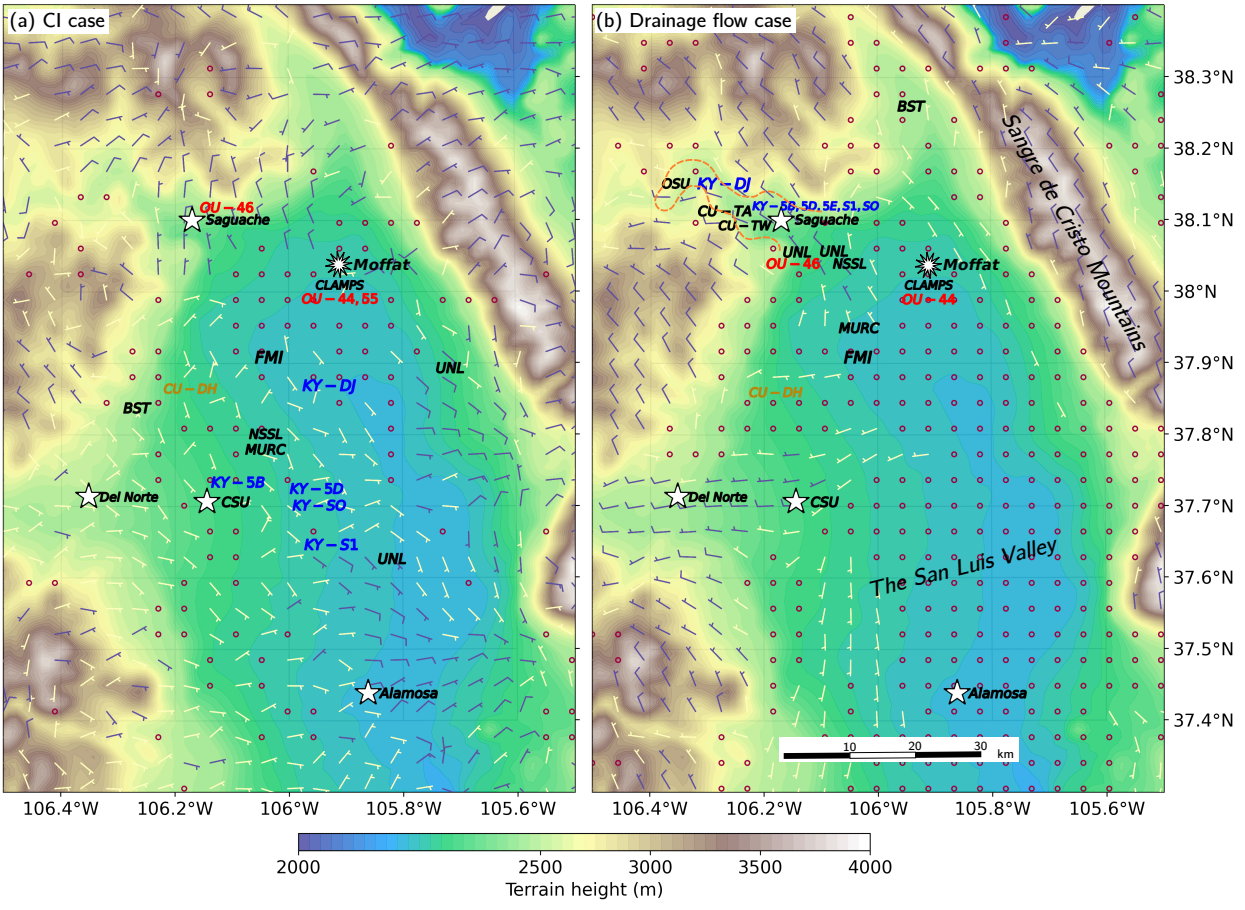

FIG. 1. Terrain map of San Luis Valley showing the platform locations during (a) the CI case on 15 July 2018 and (b) the drainage flow case on 19 July 2018. The color fill shows terrain heights with San Juan Mountains to the west and Sangre de Cristo Mountains to the east. Wind barbs at 100 m AGL obtained from realtime 1-km WRF run (see Pinto et al. 2021) are shown at 1900 UTC in (a) and 1130 UTC in (b). The wind barbs are color coded to indicate wind speeds of $1-5$ m s^{-1} (yellow) and $5-10$ m s^{-1} (blue). Red open circles indicate wind speeds of < 1 m s^{-1}. The locations of assimilated UAS observations are labeled in red, orange and blue text and discussed in Tables 1 and 2. Existing surface meteorological station locations used in the DA experiments are marked with white stars with details given in Table 3. Additional observations used for verification are labeled in black text (see Tables 1, 2, and 3). The location of Moffat is marked with a dodecagram. The dashed orange contour in (b) outlines Saguache Canyon.

moisture associated with the North American Monsoon (e.g., Higgins et al. 1999). Concurrently, a surface-based cold front approached the SLV from the north. The approaching cold front stalled

Accepted for publication in *Monthly Weather Review*. DOI 10.1175/MWR-D-22-0090.1.

TABLE 1. Summary of UAS platforms and locations for the 15 July 2018 convection initiation case.

UAS Airframe	Operating Period (UTC)	Profiling Method*	Profile Interval (min)	Max Height (m AGL)	Mean Lat/Lon	Legend Label[&]
KY BCT5B	1505-1820	Spiral: 1 km	60	990	37.711, -106.090	**KY-5B**
KY BCT5D	1430-1945	Spiral: 1 km	60	1000	37.715, -105.951	**KY-5D**
KY DJI M600	1330-2015	Up/Down	30	540	37.867, -105.929	**KY-DJ**
KY S1000	1415-1615	Up/Down	60	910	38.094, -106.162	**KY-S1**
KY SOLOW	1400-1915	Up/Down	60	310	38.094, -106.162	**KY-SO**
OU Coptersonde2	1545-1610	Up Only	15	925	37.997, -105.912	**OU-44**
OU Coptersonde2	1345-1925	Up Only	30	925	38.099, -106.170	**OU-46**
OU Coptersonde2	1325-2000	Up Only	15-30	925	37.997, -105.912	**OU-55**
CU Datahawk2	1430-1815	Spiral: 0.5 km	5	210	37.864, -106.176	**CU-DH**
BST S1	1400-2000	Spiral: 0.5 km	30	700	37.841, -106.267	BST
UNL MR6P1	1500-2100	Up/Down	30	500	37.627,-105.820	UNL
UNL MR6P2	1500-2100	Up/Down	30	500	37.893,-105.716	UNL

*Step = horizontal transects of given length with short ascents at the end of each transect; Up/Down = vertical profile straight up and down; Spiral = upward and downward spirals flown with given radius.
[&]Legend labels in bold font indicate which UAS observations were assimilated.

TABLE 2. Summary of UAS platforms and locations for the 19 July 2018 drainage flow case.

UAS Airframe	Operating Period (UTC)	Profiling Method*	Profile Interval (min)	Max Height (m AGL)	Mean Lat/Lon	Legend Label[&]
KY BCT5B	1250-1640	Step: 2.3 km	NA	125-200	38.094, -106.164	**KY-5B**
KY BCT5D	1200-1640	Step: 3.5 km	NA	175-425	38.094, -106.164	**KY-5D**
KY BCT5E	1245-1540	Step: 2.1 km	NA	150	38.094, -106.164	**KY-5E**
KY DJI M600	1130-1715	Step: 1.3 km	NA	270	38.150, -106.272	**KY-DJ**
KY S1000	1210-1715	Up/Down	60	310	38.094, -106.162	**KY-S1**
KY SOLOW	1130-1645	Up/Down	2	120	38.094, -106.162	**KY-SO**
OU Coptersonde2	1245-1715	Up Only	15	925	37.997, -105.912	**OU-44**
OU Coptersonde2	1130-1715	Up Only	15	925	38.036, -106.113	**OU-46**
CU Datahawk2	1430-1815	Spiral: 0.5 km	5	350	37.864, -106.176	**CU-DH**
CU-TALON	1220-1705	Spiral: 0.5 km	30-60	350	38.107, -106.246	CU-TA
CU-TTWISTOR	1200-1700	Stepped-Spirals: 0.8 km	30	125-300	38.103, -106.186	CU-TW
OSU SOLO-I	1226-1715	Up/Down	10	450	38.036, -106.133	OSU
BST S1	1200-1400	Stepped-Spirals: 0.8 km	10	330	38.266, -105.944	BST
FMI PRKL2	1145-1645	Up/Down	30-45	360	37.909, -106.035	FMI
UNL MR6P1	1135-1705	Up/Down	15	300	38.052, -106.103	UNL
UNL MR6P2	1150-1705	Up/Down	15	300	38.052, -106.088	UNL

*Step = horizontal transects of given length with short ascents at the end of each transect; Up/Down = vertical profile straight up and down; Spiral = upward and downward spirals flown with given radius.
[&]Legend labels in bold font indicate which UAS observations were assimilated.

within the northern portion of the SLV, helping to initiate moist convection over the higher terrain by mid-morning.

Satellite imagery indicated that clouds began building over the Sangre de Cristo Mountains and Rio Grande National Forest by 1500 UTC with deep moist convection already occurring by 1700 UTC (Fig. 2a). The strong outflows that originated over the Sangre de Cristo Mountains to the east of the SLV reached Moffat around 1915 UTC. Easterly outflow winds exceeding 12 m s^{-1} were observed with the Collaborative Lower Atmospheric Mobile Profiling System (CLAMPS) Doppler

TABLE 3. Summary of non-UAS meteorological observations used in study.

Station Identifier	Location	Station Type	Elevation (m MSL)	Latitude, Longitude	Raw Data Frequency (s)	PTRH/U Height (m)
MURC-0715	Leach	CU Tower	2322	37.782, -106.042	1	18
MURC-0719	N. Farm	CU Tower	2325	37.951, -106.033	1	18
Doppler lidar	Saguache Airport	CU Windcube	2393	38.907, -106.169	1	40-220
Doppler lidar	Moffat	CU Windcube	2305	37.998, -105.912	1	40-220
CLAMPS-1	Moffat	Sondes	2305	37.998, -105.912	< 1	SNDG
CLAMPS-1	Moffat	Sfc Station	2305	37.998, -105.912	1	3/NA
CLAMPS-1	Moffat	Lidar Profiler	2305	37.998, -105.912	1	75-2000
CoMet-1-0715	Mobile	Sfc Station	NA	NA	1	2.5/3.25
CoMet-1-0719	Mobile	Sfc Station	NA	NA	1	2.5/3.25
CoMet-2-0715	Fixed	Sfc Station	2330	37.893, -105.716	1	2.5/3.25
CoMet-2-0719	Fixed	Sfc Station	2330	38.058, -106.087	1	2.5/3.25
KALS	Alamosa	ASOS	2298	37.435, -105.867	60	2/10
K04V	Saguache Airport	AWOS IIIP	2393	38.097, -106.169	1200	2/10
KRCV	Del Norte	AWOS IIIP/T	2425	37.714, -106.352	1200	2/10
CSU	Center	CSU AgMet	2348	37.707, -106.144	3600	2
KMYP	Monarch Pass	AWOS IIIP/T	3666	39.497, -106.320	3600	2/10
NSSL Sondes-0715	Leach	NSSL M-Mesonet	2322	37.782, -106.042	< 1	SNDG
NSSL Sondes-0719	N. Farm	NSSL M-Mesonet	2313	38.053, -106.051	< 1	SNDG
FMI-0715	CR53N	TriSonica Sfc Met	2310	37.909, -106.035	60	2.75

lidar up to 1.5 km AGL at Moffat (Fig. 3b, c) and were accompanied by 8°C of cooling at the surface (Fig. 3a). Low-level convergence associated with this outflow boundary resulted in rapid development of a line of cumulonimbus clouds as is clearly evident in a photo taken 10 min after outflow boundary passage (Fig. 4, note the wind-bent trees). By 2000 UTC, a strong convective cell had initiated just north of Moffat as indicated in the WSR-88D composite radar reflectivity field with values exceeding 40 dBZ. The CLAMPS was at the southern edge of this storm cell with only light precipitation being recorded there (Fig. 3a). The convective precipitation to the north produced an additional outflow moved through Moffat around 2000 UTC and resulted in a deepening layer of northerly winds (Fig. 3c). By 2030 UTC, the north-south line of deep moist convection filled the center of the SLV as evidenced by the visible satellite imagery with radar echos being detected near Alamosa and Moffat. Note that the radar likely underrepresented the full extent of precipitation due to radar-beam blockage below 10,000 ft within the SLV (Martinaitis et al. 2020).

b. Drainage flow case

Cold air flowed out of Saguache Canyon every morning during LAPSE-RATE. These drainage flows varied in both strength and duration and ultimately succumbed to up-canyon flows after sunrise (see Pinto et al. 2021). A detailed description of the drainage flow observed on 19 July

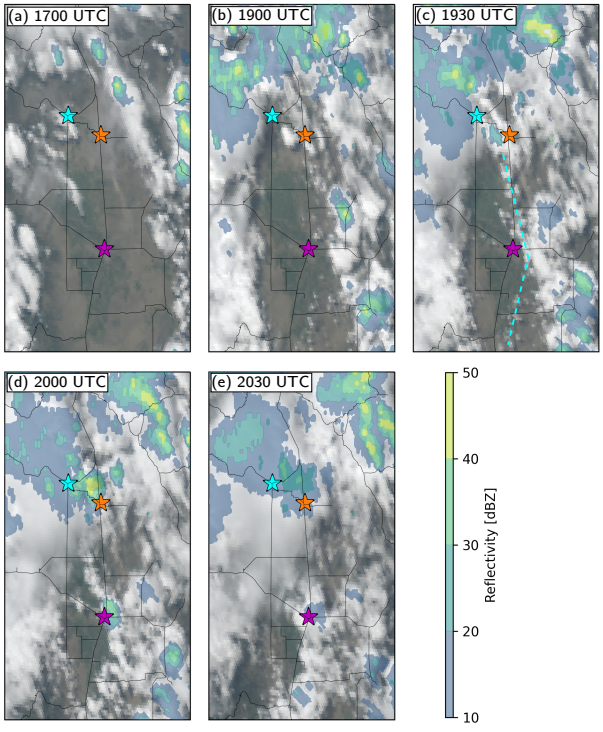

FIG. 2. Visible satellite image and composite radar reflectivity (NEXRAD) depicting the evolution of convection at (a) 1700, (b) 1900, (c) 1930, (d) 2000, and (e) 2030 UTC for the CI case on 15 July 2018. The cyan, orange, and magenta stars mark the locations of Saguache, Moffat, and Alamosa, respectively. The dashed cyan lines in (c) show the location of outflow boundaries derived based on the organization of the incipient cumulus clouds. Main roads within the SLV are indicated by the black lines.

2018 at Saguache is given in Jensen et al. (2021). Additional terrain-driven flows were observed at Moffat on this day (Fig. 3e, f) where east-northeasterly winds develop around 0600 UTC and persist until 1600 UTC beneath a layer of stronger northwesterly flow. After 1600 UTC, the wind at Moffat shifts to southeasterly in response to the upvalley flow circulation that spanned much of the eastern half of the SLV. Key aspects of this diurnally varying wind system that will be assessed include the distance that canyon drainage winds extended into the valley, the timing of upvalley and up-canyon flow reversal, and the characteristics (e.g., strength, depth, and spatial extent) of the upvalley flow.

Accepted for publication in *Monthly Weather Review*. DOI 10.1175/MWR-D-22-0090.1.

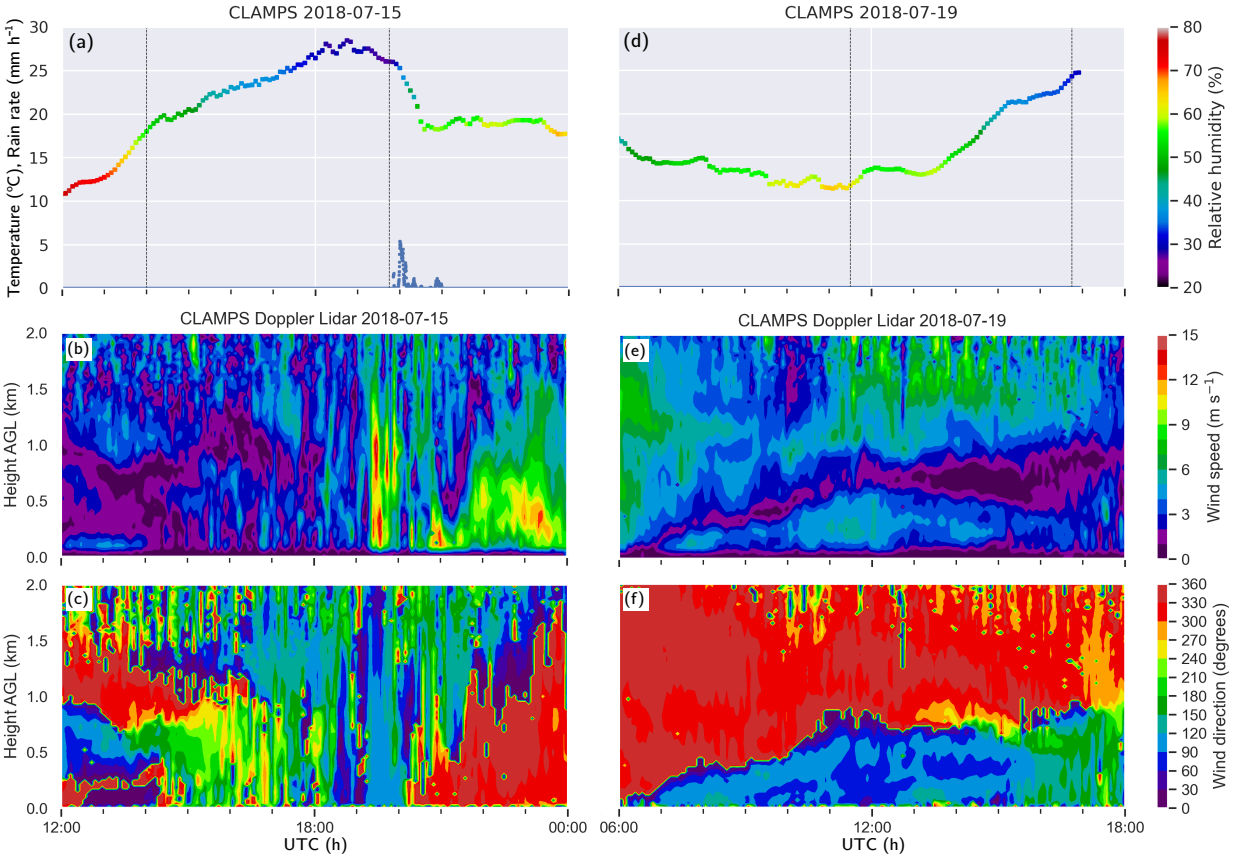

FIG. 3. Timeseries of (a, d) 2-m air temperature (ordinate) and relative humidity (denoted by the colorbar) from the CLAMPS surface meteorological station for (a) 15 July 2018 and (d) 19 July 2018. The precipitation (rain) rate from CLAMPS is also shown in (a) as the small blue points. The dashed lines in (a) and (d) bracket the UAS observation periods. Also shown are time-height cross-sections of CLAMPS Doppler lidar (b, e) wind speed and (c, f) wind direction for (b, c) 15 July 2018 and (e, f) 19 July 2018.

c. Assimilated observations

The UAS resources were deployed differently each day depending on the particular forecast problem and represent a targeted sampling approach that could be operationally implemented for improved weather prediction. For the convection initiation case, most of the UAS resources (Table 1) were deployed along a north-south line in the center of the SLV in order to capture the pre-convective environment. These UAS performed continuous profiling up to 900 m AGL between 1400 and 2000 UTC. Additional profiling sites were located near the foothills of the San

Accepted for publication in *Monthly Weather Review*. DOI 10.1175/MWR-D-22-0090.1.

FIG. 4. Photo taken facing north at the Moffat observing site at 1925 UTC during CI case on 15 July 2018. Linear organization of lowered convective cloud bases denotes location and orientation of strong low-level convergence. The strong easterlies at Moffat can be inferred from the direction of the bent tree branches. The CLAMPS trailer is on the basketball court behind the trees.

Juan and Sangre De Cristo Mountains to capture any storm outflows that originated over higher terrain to the west and east, respectively (Fig. 1a). For the drainage flow case, targeted UAS flights were primarily flown within and at the mouth of Saguache Canyon (Fig. 1b). Details of this case and associated deployment strategies are given in Jensen et al. (2021) and the resources are summarized in Table 2. Data quality was assessed for all UAS platforms by Barbieri et al. (2019) and those with the largest biases were not utilized in this study. Of the remaining high quality UAS observations, only a subset were assimilated with the rest being withheld for model verification.

Only four permanent surface meteorological stations are available within the SLV for DA. These stations represent observations that are conventionally available within the SLV. They are located in Alamosa (KALS), Saguache (K04V), Del Norte (KRCV) and Center (CSU). A summary of

Accepted for publication in *Monthly Weather Review*. DOI 10.1175/MWR-D-22-0090.1.

each surface meteorological station used in this study is given in Table 3. All of these stations are located in the western half of the SLV, far removed from the Sangre de Cristo Mountains where key processes that impacted the evolution of both the CI and drainage flow cases occurred.

d. Independent observations used for evaluation

Data from additional observing systems deployed during LAPSE-RATE are used to independently evaluate the priors, analyses and forecasts generated for each OSE. The National Severe Storms Laboratory (NSSL) mobile sounding system (labeled NSSL in Fig. 1) launched radiosondes at Leach Airport during the CI case and at the North Farm location during the drainage flow case. Soundings were also launched from the CLAMPS trailer at Moffat on both days. The University of Colorado Mobile UAS Research Collaboratory (MURC) and the two University of Nebraska-Lincoln (UNL) mobile mesonet (Integrated Mesonet and Tracker (CoMet-2)) vehicles were also positioned in different locations for the two cases (see Fig. 1 for locations). These observations are described in Table 3. Finally, observations from several UAS that were flown in remote parts of the SLV (see Tables 1 and 2) were withheld to evaluate the resulting analyses and predictions at locations far removed from the other independent observations. While model evaluation is difficult because of the general lack of observations in the SLV, these observing systems were critical for expanding the independent truth dataset.

Surface-based remote sensing platforms were deployed at Saguache Municipal Airport and Moffat. Leosphere WindCUBE v1 Doppler lidar systems were deployed at Saguache and Moffat. In addition, a higher-power Doppler lidar included as part of the Oklahoma University/NSSL Collaborative Lower Atmospheric Mobile Profiling System (CLAMPS-1) was sited at Moffat. The WindCUBE Doppler Lidar has a range of $40-200$ m with a vertical resolution of 20 m while the CLAMPS-1 Doppler Lidar was configured to have a range of $75-2000$ m and a vertical resolution of 30 m (Table 3).

3. Ensemble data assimilation

The impact of UAS in addition to surface meteorological observations on the skill of analyses and forecasts is assessed using regional OSEs. The experiments are conducted using a modified version of the Manhattan release of the Ensemble Adjustment Kalman Filter (EAKF) data assimilation

system available in NCAR's Data Assimilation Research Testbed (DART, Anderson 2001). Key aspects of the DA system are given below with more details provided by Jensen et al. (2021). .

a. DA system configuration and settings

The DART EAKF DA system has been adapted to assimilate UAS observations using a nested configuration (1 km grid nest within a 3 km grid) of the Weather Research and Forecasting (WRF) model (Skamarock et al. 2008) version 3.9.1.1. A 15-min cycling period and 40-member ensemble were used to assimilate surface and UAS observations into the 1-km grid. Observations were not assimilated into the 3-km grid mesh (not shown) which spanned the western half of the United States. Horizontal localization values were specified to be 127 km for UAS observations and 382 km for the surface meteorological station observations. Vertical localization values of 333 m and 1 km were used for UAS and surface observations, respectively. The horizontal localization used for surface observations was based, in part, on the work of Pu et al. (2013) who found an optimal horizontal localization distance in complex terrain of 320 km. Using a larger radius of influence for the surface observations is also consistent with their relatively wide spacing within the SLV. The shallow vertical localization used for the surface observations was chosen to reduce potentially deleterious impacts of extending near-surface measurements within an environment characterized by complex vertical structures. Since the UAS observations are closer together, a smaller localization radius is used as discussed in Jensen et al. (2021).

Observational error covariances for surface observations and UAS were determined based on previous studies and are given in Table 4 for reference. The UAS observation error variances are based on those used to assimilate observations from commercial aircraft with slight adjustments to the previously used values as guided by the UAS observation error assessment of Barbieri et al. (2019). Because of the density of UAS observations in some locations, they have been superobbed using a horizontal radius of 2 km and a depth of 3 hPa (~30 m). Superobbing is often used to upscale observations in regions where the observational dataset has finer spatial resolution than the model (Torn and Hakim 2008).

Initial and lateral boundary conditions for the two cases were obtained from the 0400 UTC forecast cycle of the High-Resolution Rapid Refresh (HRRR, Benjamin et al. 2016). The 40-member ensemble is generated by adding perturbations to both the 3 km and 1 km WRF grids

TABLE 4. Observation error variances.

Observation Type	Temperature $(K)^2$	RH $(\%)^2$	Wind $(m\ s^{-1})^2$	Reference
SFC	1.5	5.0	1.5	Ha and Snyder (2014)
UAS	1.0	3.0	1.0	Dirren et al. (2007)

using generic background error statistics (WRFDA CV3, Parrish and Derber 1992). Following Benjamin et al. (2016), perturbations were also added to the soil moisture and soil temperature in order to prevent loss of ensemble spread in the lower atmosphere as described in Jensen et al. (2021). The 40 ensemble members were then spun up until the first UAS observations were available. The spin-up period ran from 0400 – 1130 and 0400 – 1400 UTC for the drainage and CI cases, respectively, due to the timing of when UAS operations commenced. Note that in both cases, SFC DA was only turned on once UAS observations became available. The DA period ran from 1130 – 1645 and 1400 – 1945 UTC for the drainage and CI cases, respectively.

b. DA experiments

OSEs were conducted to quantify the relative benefit of assimilating UAS observations in addition to conventional surface observations (UAS+SFC DA) over that obtained with assimilating surface observations (SFC DA) alone in a relatively data sparse region characterized by complex mesogamma-scale flow patterns. An additional reference experiment with no data assimilation (noDA) was also run (see Fig. 7). The impact is assessed by using independent observations to evaluate the skill of successive ensemble mean analyses and subsequent free forecasts initialized using these ensemble mean analyses for both the UAS+SFC DA and SFC DA experiments.

4. Assessment of UAS data assimilation on the ensemble mean analyses

Quantifying changes in the skill of the analyses and predictions that result from assimilating a particular dataset is critical for determining the potential value of a new observing system prior to its widespread adoption. For simplicity, only the difference between the assimilation of surface observations and surface plus UAS observations is considered in this study. It is noted that the potential impact of other conventional observations is expected to be small in these two cases because of the shallow and small scale nature of the relevant processes which would not be captured by other far-removed conventional observations (e.g., radiosonde soundings, aircraft profiles). The

impact of adding UAS observations to and existing surface observing network to the skill of the ensemble mean analyses is discussed below for both the terrain-driven flow and CI case.

a. Impact of UAS observations on analyses of the terrain-driven flows

Ensemble mean analyses for the drainage flow case were generated at successive 15-min intervals from 1130 to 1645 UTC. The ensemble mean analyses of potential temperature (θ), moisture and winds at 300 m AGL that were generated after 1.5 h of cycling are shown in Figs. 5 and 6 for both SFC and UAS+SFC DA experiments valid at 1300 UTC. Independent observations obtained at 300 m AGL from multiple UAS and the two radiosonde launches at 1300 UTC are overlaid for comparison. In general, the UAS+SFC analysis is warmer than the SFC analysis at this time and altitude, but the details of the differences are complex. In the UAS+SFC DA simulation, the northwestern quadrant of the SLV warms with θ being closer to the independent observations (Fig. 5c) while the coldest region shifts from the mouth of the Saguache Canyon in the SFC DA run to being located to the south and east of Moffat in the UAS+SFC run. This pattern generally fits the independent observations better than that obtained with SFC DA (Fig. 5a); however, details of the differences between the two runs are complex. For example, independent observations within Saguache Canyon indicate that the SFC DA results resulted in the cold pool being too deep within the canyon. This bias is notably reduced with the addition of UAS observations to the assimilation. It is also noted that, the UAS+SFC DA is generally warmer along the edges of the SLV than the SFC DA run. This warmer solution is also more consistent with the independent UAS observation obtained in the northernmost inlet of the SLV (Fig. 5a, c).

The UAS observations also had a positive impact on the analysis of moisture at 300 m AGL. The ensemble mean analysis obtained with SFC DA indicates a crescent of higher water vapor mixing ratio (q_v) that pooled across the western third of the SLV (Fig. 5b). The addition of UAS observations increases q_v across much of the eastern and central SLV which nudges the moisture values closer to the two independent truth values that were farthest from the Saguache Canyon (Fig. 5d). The UAS observations increased moisture within the northern canyons and across much of the adjacent foothills. The increased moisture in Saguache Canyon is an improvement over the drier values obtained with SFC DA. As with biases evident in the 300 m potential temperature,

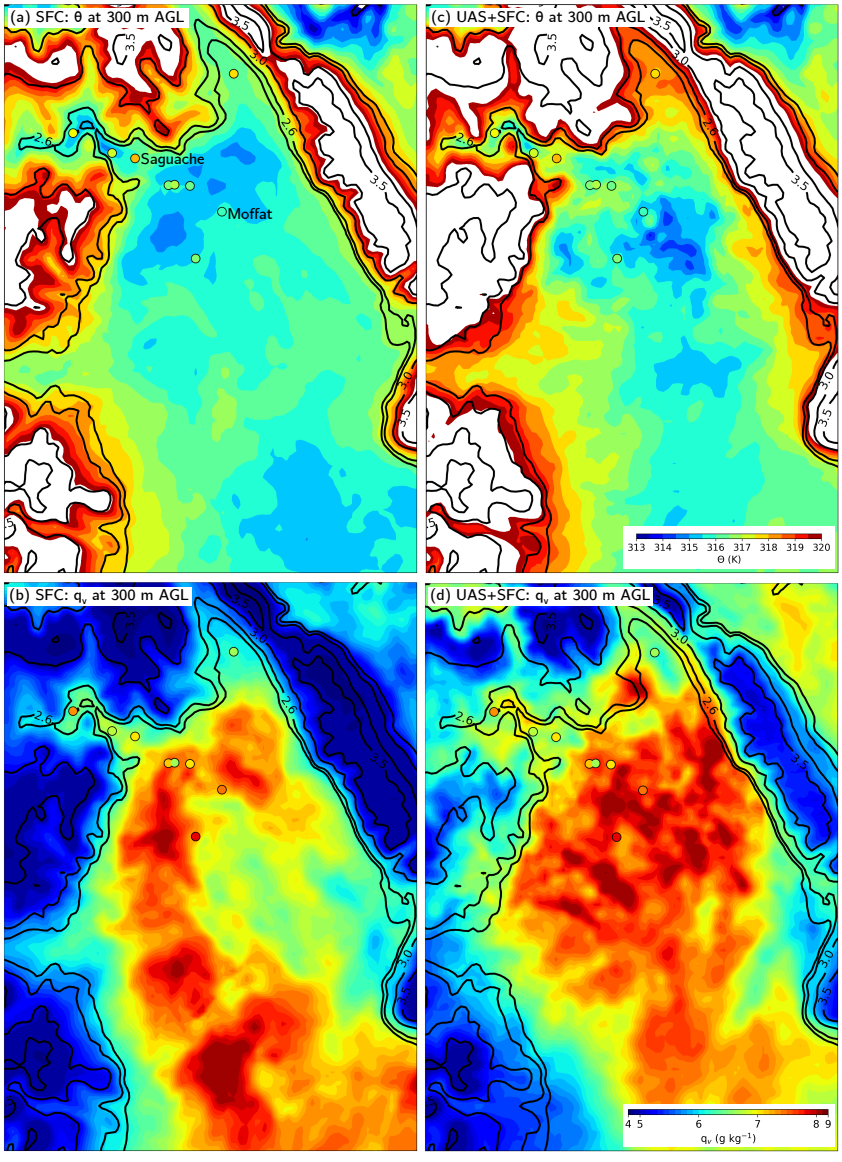

FIG. 5. Ensemble mean analyses of (a, c) θ and (b, d) q_v at 300 m AGL obtained for (a, b) SFC and (c, d) UAS+SFC DA experiments valid at 1300 UTC on 19 July 2018 during the drainage flow case. Values from independent UAS and radiosondes (both averaged from 295 – 305 m AGL) are shown as the filled circles using the color scale given by the legend. White regions in (a) and (c) are for θ values above 320 K. The unevenly spaced color values in (b) and (d) are used to highlight the differences in the q_v values in the SLV and attendant canyons. Black contours indicate terrain heights of 2.4, 2.6, 3.0 and 3.5 km MSL.

the surface moisture observations obtained with the surface meteorological station at Saguache Airport was not representative of the conditions well above the surface.

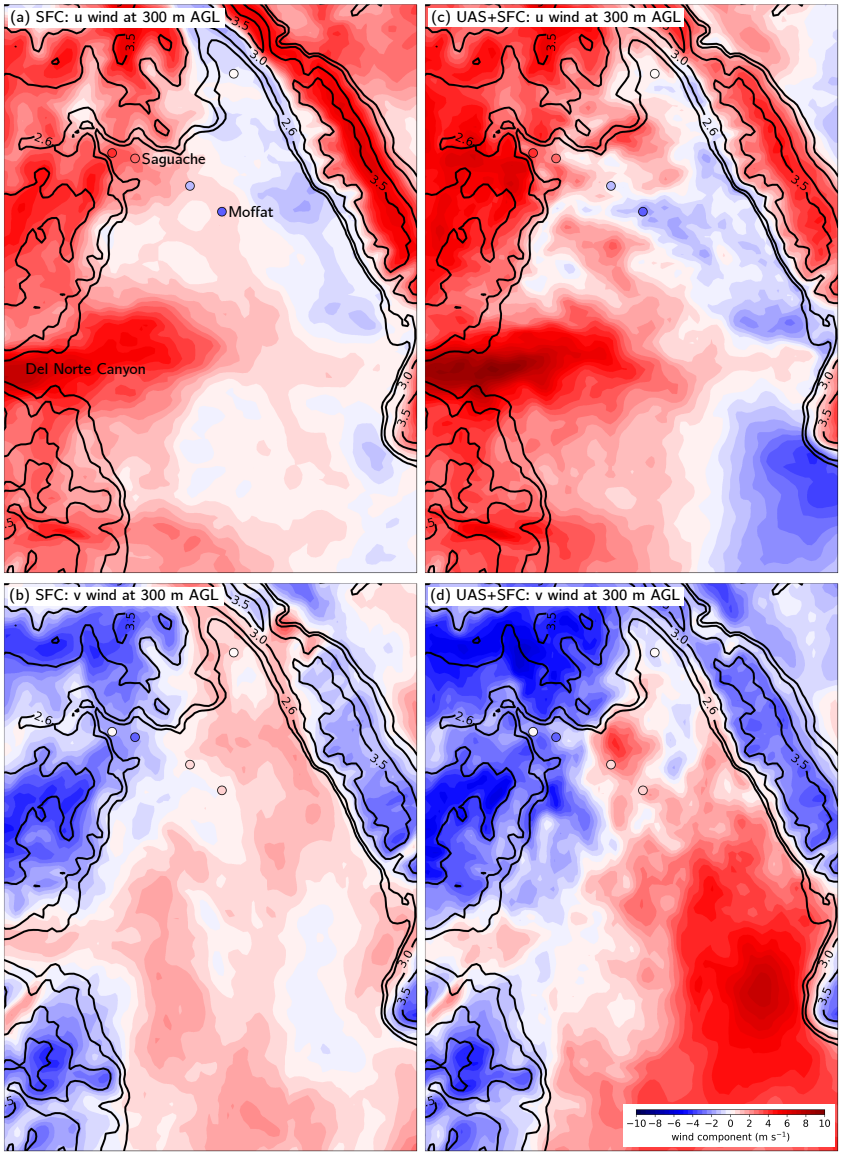

FIG. 6. Same as in Fig. 5 except for the (a, c) u-wind and (b, d) v-wind components at 300 m AGL. Note that there are fewer observations than in Fig. 5 because several UAS did not measure winds.

Finally, the UAS observations had a positive impact on the wind field at 300 m AGL. The ensemble mean winds obtained with both DA experiments depict a strong westerly jet emanating from Del Norte Canyon and a weaker northwesterly flow from Saguache Canyon at 1300 UTC (Fig. 6). The flow from Del Norte Canyon is actually stronger in the UAS+SFC run while the flow from Saguache Canyon spans a much smaller area in the UAS+SFC run. In addition, the UAS+SFC

wind analysis agrees well with independent observations in the northern SLV that indicate a wind shift (from northwesterly to southeasterly) just beyond the mouth of the Saguache Canyon. The UAS+SFC DA correctly captures the southeasterly flow at Moffat (Fig. 6c) while the SFC DA run has northwesterlies at both sites (Fig. 6a). Interestingly, there is also a strong response in the flow field in the southern half of the SLV, with weak northwesterly flow in the SFC DA run being replaced by stronger southeasterly flow in the UAS+SFC DA run. Unfortunately, independent observations were not available in this region. As will be discussed further below, this major difference between the two analyses is in response to changes in the north-south thermal gradients across the SLV which improves the overall depiction of terrain-driven flows across the SLV.

An example of the improved thermal structure obtained with UAS+SFC DA is given in Fig. 7. The 1300 UTC sounding obtained at Moffat reveals the presence of a strong (15 K) and deep surface-based inversion. The UAS+SFC DA run better captures the vertical structure of the inversion with most of the θ deficit being confined below 2500 m MSL (200 m AGL) as observed. In the SFC DA run, the θ deficit is spread over a much deeper layer resulting in a deep layer of biases < -1.5 K which is greater than that obtained in a simulation in which no data were assimilated (noDA). This again points to the challenges associated with spreading the influence of surface observations vertically under conditions characterized by complex vertical structure. While UAS+SFC DA introduces a small cold bias in the lowest 200 m AGL (below 2500 m MSL), the magnitude of the bias above that is greatly reduced up to 4000 m MSL which corresponds with UAS profiling height plus the vertical localization distance of 1000 m.

The improvements in θ discussed above are representative of those found across the northern half of the SLV. Figure 8 provides a comparison of west-to-east cross-sections of data obtained from the ensemble mean analyses with observations from two radiosonde launches located 15 km apart (NSSL mobile and Moffat). Again, the stability of the lower atmosphere is better represented across the northern portion of the SLV in the UAS+SFC run. The improvements in UAS+SFC are evident primarily as colder θ values at low levels and warmer θ values aloft, in better agreement with the radiosonde measurements. The UAS+SFC DA also improves the analysis of horizontal winds across the northern portion of the SLV. Radiosonde observations indicate that southeasterly winds extend at least 15 km to the east of Moffat and up to 3000 m MSL at Moffat. The UAS+SFC DA analysis (Fig. 8b) captures the depth and area covered by south-southeasterlies much better than

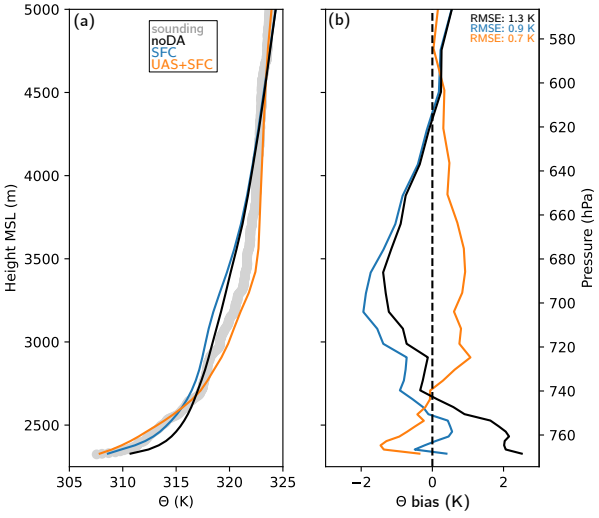

FIG. 7. Mean profiles of (a) θ and (b) θ bias (model – observation) obtained from 40 analyses valid at 1300 UTC on 19 July 2018 (drainage flow case). Profiles in (a) are from the noDA (black), SFC (blue), and UAS+SFC (orange) DA experiments with radiosonde observations given by the thick gray line. Model profiles of θ represent the ensemble mean of the analyses averaged over a latitudinal band that ranges from 106.0°W to 105.8°W centered on Moffat (37.998°N, 105.912°W). RMSEs in (b) are calculated using model levels from the surface to 5000 m MSL for this single evaluation time.

the SFC DA run (Fig. 8a) as indicated via comparison of the model-derived wind shift boundary in the analyses (dashed yellow line) and the radiosonde low-level southeasterly winds.

As indicated earlier, improvements in the analysis of potential temperature (Figs. 5 and 8) in the UAS+SFC DA run led to improvements in the mesoscale flow pattern observed on this day. The UAS+SFC run has sharper horizontal θ gradients than the SFC run with warmer regions being evident adjacent to the mountains and within the three major inlet canyons (Fig. 9). In opposition to the SFC run, the northern portion of the SLV is notably warmer than the southern portion of the SLV in the UAS+SFC DA run. This gradient reversal between the two DA experiments promotes upvalley flow which is evident throughout most of the eastern half of the SLV in the UAS+SFC DA run (Fig. 9). The impact of this gradient reversal on the horizontal wind field is in agreement with that discussed by (Wagner et al. 2015) who demonstrated that upvalley flow is enhanced when the potential temperature gradient aligns with the slope of the terrain (i.e., higher terrain to the north in this case).

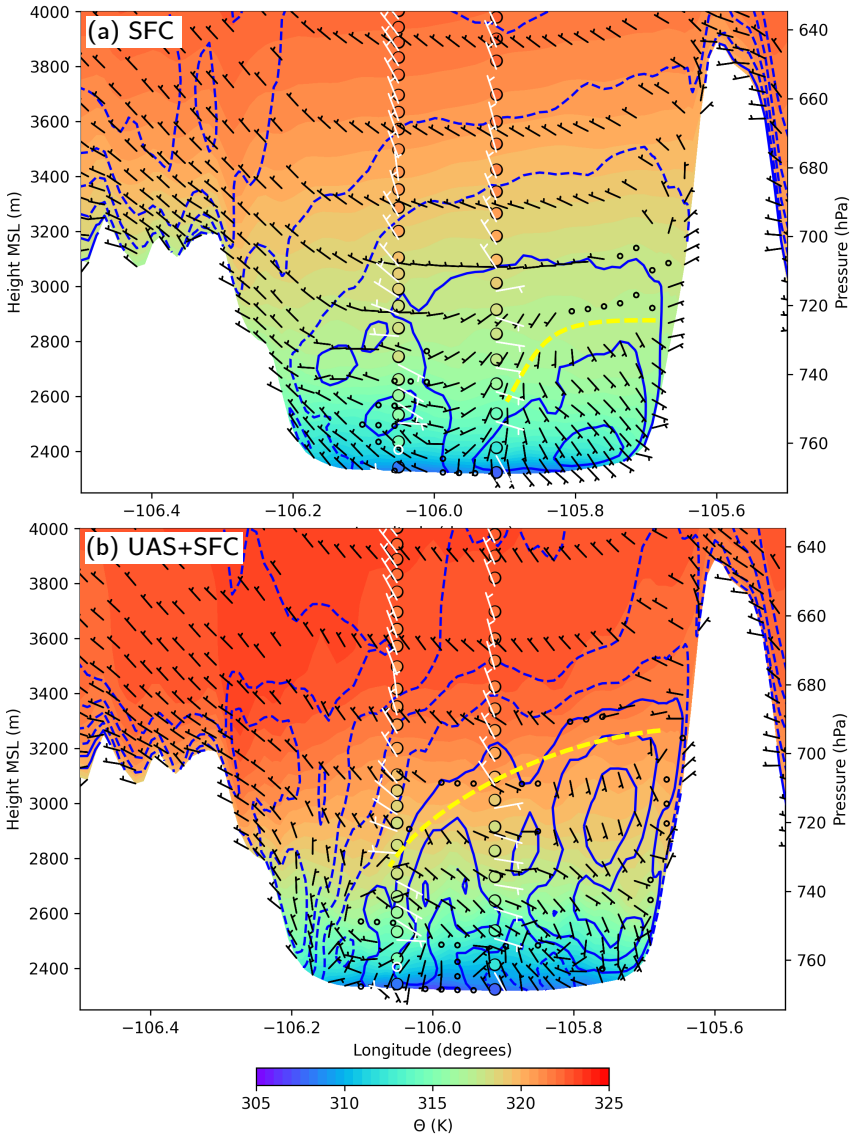

FIG. 8. West-to-east cross-section of winds and θ obtained from ensemble mean of the analyses valid at 1300 UTC (19 July 2018) from (a) SFC and (b) UAS+SFC centered on Moffat (38°N). The black wind barb half flags indicate values of at least 1 m s^{-1} with the orientation of the barbs indicating the horizontal wind flow direction. The v-wind component is also contoured in blue from −4 to 4 by 2 m s^{-1} (negative is dashed). θ from the soundings at Moffat (38.00°N, 105.91°W) and the NSSL mobile mesonet sounding (38.05°N, 106.05°W) are shown as color-filled circles and wind barbs are show in white (u-v components shown). The yellow dashed lines show the top of the southeasterly winds in each analysis.

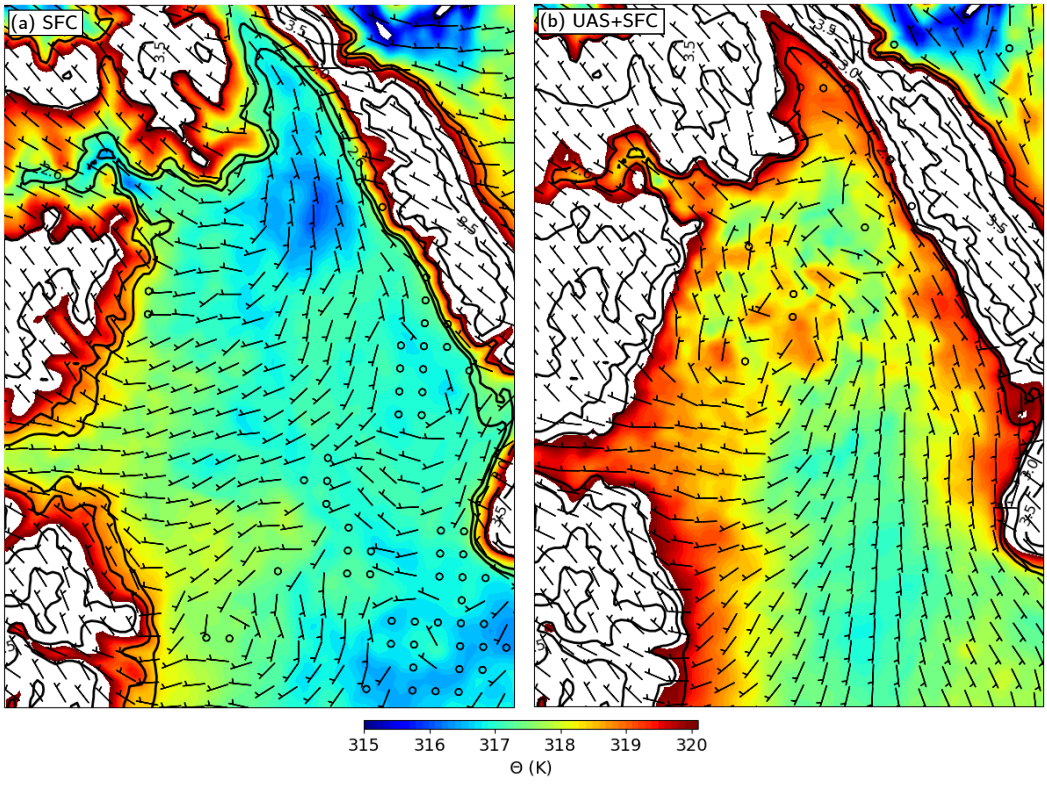

FIG. 9. Ensemble mean of θ and wind barbs obtained at 450 m AGL obtained from the priors valid at 1300 UTC on 19 July 2018 from the (a) SFC and (b) UAS + SFC experiments. White fill indicates regions were θ was above 320 K. Open circles indicate wind speed < 1 m s^{-1}. Black contours indicate terrain heights of 2.4, 2.6, 3.0 and 3.5 km MSL.

b. Impact of UAS observations on analyses of the convection initiation case

Analyses for the CI case (15 July 2018) were generated at successive 15-min intervals from 1400 to 1945 UTC. The impact of UAS observations on the 300-m θ and q_v analyses at 1700 UTC is shown in Fig. 10. Generally, compared with SFC DA, the 300-m analyses obtained with UAS+SFC DA are cooler and drier in the center of the SLV but warmer and more moist over the surrounding higher terrain. Comparison with independent observations available within the SLV reveals that while biases in θ are similar, there are much stronger north-south and east-west gradients in the UAS+SFC DA experiment (Fig. 10a, c). These gradients may play a role in the development of convection in the center of the SLV on this day. The SFC DA analysis is too moist in the center of

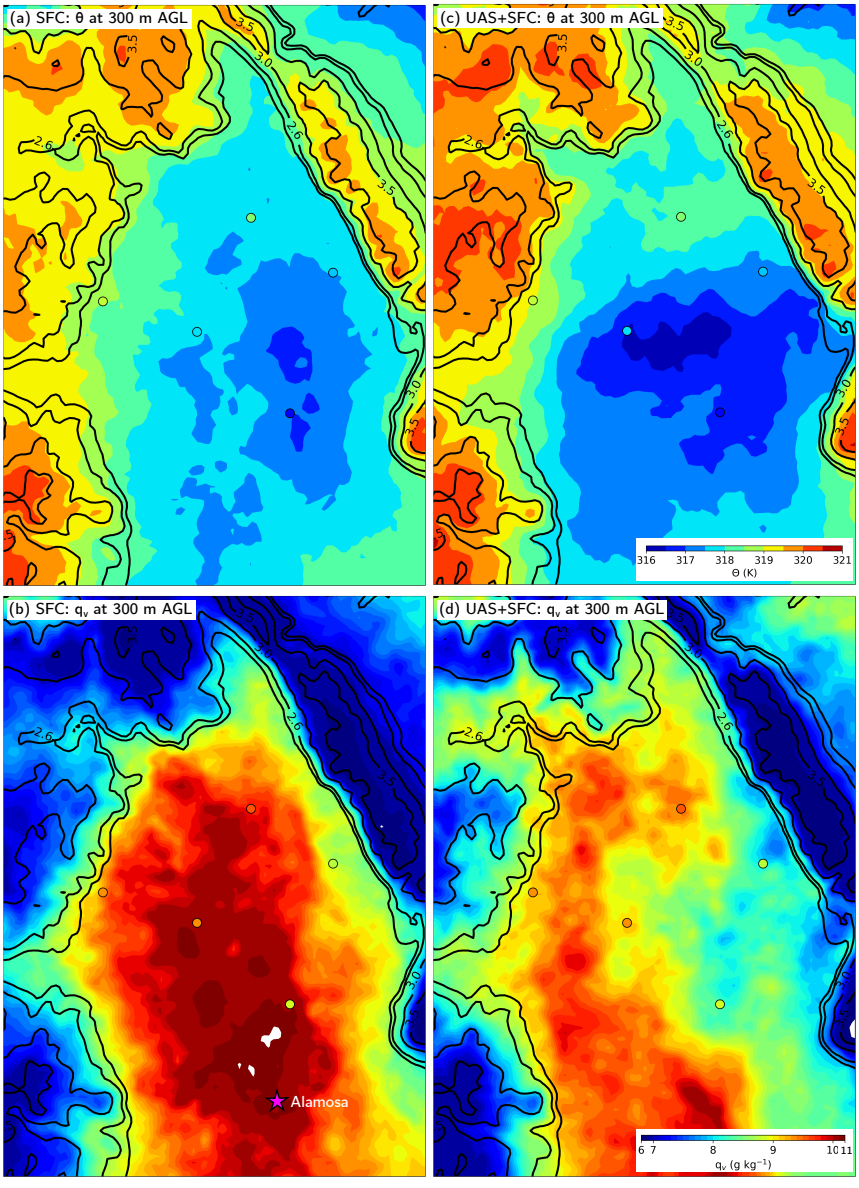

FIG. 10. Same as in Figure 5 except analyses are for the convection initiation case at 1700 UTC on 15 July 2018. White regions in (b) are for q_v values greater than 11 g kg^{-1}. The unevenly spaced color values in (b) and (d) are used to highlight q_v differences between the two experiments.

the SLV compared to the independent observations (Fig. 10b) with a moist bias of nearly 3 g kg^{-1} near Alamosa.

As will be discussed below, despite this excess low-level moisture in the SFC DA experiment, the SFC DA simulations fail to produce CI in the center of the valley. In contrast, the UAS+SFC

Accepted for publication in *Monthly Weather Review*. DOI 10.1175/MWR-D-22-0090.1.

experiment is generally much drier throughout the SLV with a slight dry bias being evident across the southeastern portion of the SLV. At the same time, UAS+SFC DA results in more moist conditions over the elevated terrain to the west and north of the SLV. These more moist conditions over the foothills, which are clearly evident in and around Saguache Canyon, were critical to the initiation of convection over the foothills. As will be discussed below, outflows from these initial convective storms propagated into the SLV and ultimately led to CI in the north-central part of the SLV.

Equally critical improvements were found in vertical profiles of moisture afforded by UAS+SFC DA (Fig. 11). Both DA experiments generally capture the temperature profile but miss the moist layers centered at 450 and 550 hPA at both 1530 and 1730 UTC. Both simulations are also too moist between 300 and 400 hPA falsely indicating the presence of high cirrus cloud layer that was not observed at this time. Nonetheless, the moisture profiles obtained in the UAS+DA run were improved relative to that obtained with the SFC DA run with an increased dewpoint temperature between the surface and 525 hPa (2950 m AGL) at 1530 UTC. In particular, the UAS+SFC simulation better captures the amount of moisture within the developing mixed layer observed at 1530 UTC. In fact, the assimilation of UAS observations increased the dew point at 725 hPa by 2.7°C (1.9 g kg^{-1}), an increase in water vapor mixing ratio of over 25%. Interestingly, by 1730 UTC, UAS+SFC DA produce higher dewpoint temperatures up to 400 hPa (much higher than UAS flights plus the vertical localization distance). As will be discussed further below, these increases in dewpoint temperature aloft are caused by indirect effects, whereby increases in low-level moisture over the foothills of the San Juan Mountains (west of the SLV) resulted in earlier convection and subsequent moistening of mid-levels of the atmosphere that then advected over the north-central portion of the SLV resulting in increased moisture between 400 and 600 hPA. Finally, it is noted that the moist bias between 300 and 400 hPA is not reduced in either DA experiment.

The process of upper-level moistening described above is demonstrated by assessing the role of UAS+SFC DA in driving an earlier and more widespread onset of mountain-based convection initiation. As shown in Fig. 10, the addition of UAS observations to the DA increased low-level moisture and θ over the higher terrain over the foothills of the San Juan Mountains to the west of the SLV. These changes increased instability over the foothills through mid-morning local time. The impact of UAS+SFC DA on the atmospheric stability over the mountainous terrain is illustrated in

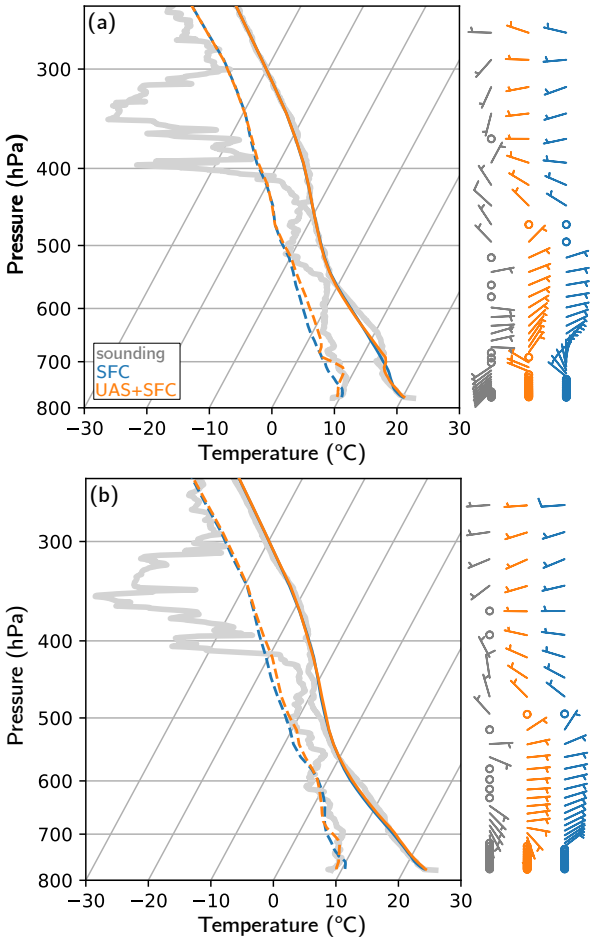

FIG. 11. Skew-T Log-P diagrams showing ensemble mean analyses of temperature (solid) and dewpoint temperature (dashed) obtained from SFC (blue) and SFC+UAS (orange) experiments at (a) 1530 UTC and (b) 1730 UTC on 15 July 2018 (CI case) from grid point closest to Moffat. The Moffat radiosonde data are shown in gray. Wind speeds are in knots with half flag representing winds of 1 – 5 knots. Note that the maximum pressure level attained by UAS was 700 hPa. Using a vertical localization distance of 1 km places the top of direct UAS DA impacts at around 600 hPa.

Fig. 12. The UAS+SFC DA results in a clear increase in q_v at terrain heights between 2.7 km and 3.6 km (MSL) at 1530 UTC (Fig. 12a). The higher water vapor mixing ratios in the UAS+SFC DA case are in better agreement with an observation of q_v (8.9 g kg^{-1}) obtained at Monarch Pass located 50 km to the north-northwest of Saguache at 3666 m MSL. The greater low-level moisture values at these elevations in the UAS+SFC DA run leads to higher CAPE, with mean values

increasing from around 200 to 400 J kg^{-1} (Fig. 12b). At the same time CIN values are slightly depressed at the same range of elevations (Fig. 12c). The mean liquid water path (LWP) values shown in Fig. 12c indicate that clouds and deep moist convection had already begun to develop in the UAS+SFC DA run at elevations of $3000 - 3400$ m by 1530 UTC whereas the SFC DA run shows no evidence of cloud cover at this time.

While it is not known exactly what triggered deep convection over the mountains on this day, the UAS+SFC DA clearly preconditioned the environment to more readily enable deep moist convection. Ultimately, convection was initiated over the center of the SLV by low-level convergence associated with a merger of outflows from storms that formed over the mountains on both sides of the SLV. In general, determining where and when these outflows will form and ultimately converge in the valley is a challenging forecast problem. While CI was occurring over the mountains, UAS profiling continued across the SLV and captured outflow passage at Moffat around 1930 UTC which was critical in determining its location and strength. The u-wind analysis increment at 1930 UTC (Fig. 13) shows the impact of UAS DA just after the outflow boundary rushed through Moffat. While the analysis increments are small and unorganized in the SFC DA run (Fig. 13a), with the exception of increased westerlies in the lee of the San Juan Mountains, evidence of the easterly outflow impacting Moffat is only seen in the UAS+SFC DA analysis increment (Fig. 13b). In addition, the UAS+SFC DA run extends the westerly outflow from Saguache Canyon into the center of the SLV. Both of these coherent increments represent the impact of the UAS observations that captured outflows emanating from convection that formed over higher terrain to the east and west of Moffat.

Comparison of the ensemble mean analyses of wind generated at 1900 and 1930 UTC from the SFC and UAS+SFC reveal substantial differences in the low-level wind field (Fig. 14). In the SFC analysis, there is evidence of stronger easterly outflows to the east of Moffat, but only weak evidence of outflows from storms over the San Juan mountains at both times. On the other hand, UAS+SFC DA indicates a much more dynamic solution with much stronger westerly outflows emanating from the San Juan Mountains that quickly propagated across the SLV. The analyzed wind field obtained with UAS+SFC DA agrees much better than SFC DA with the independent observations at both times shown. In particular, UAS+SFC DA captures the placement and timing of the outflow that impacted Moffat from the east as is evident in the observed wind shift at Moffat between 1900 and

Accepted for publication in *Monthly Weather Review*. DOI 10.1175/MWR-D-22-0090.1.

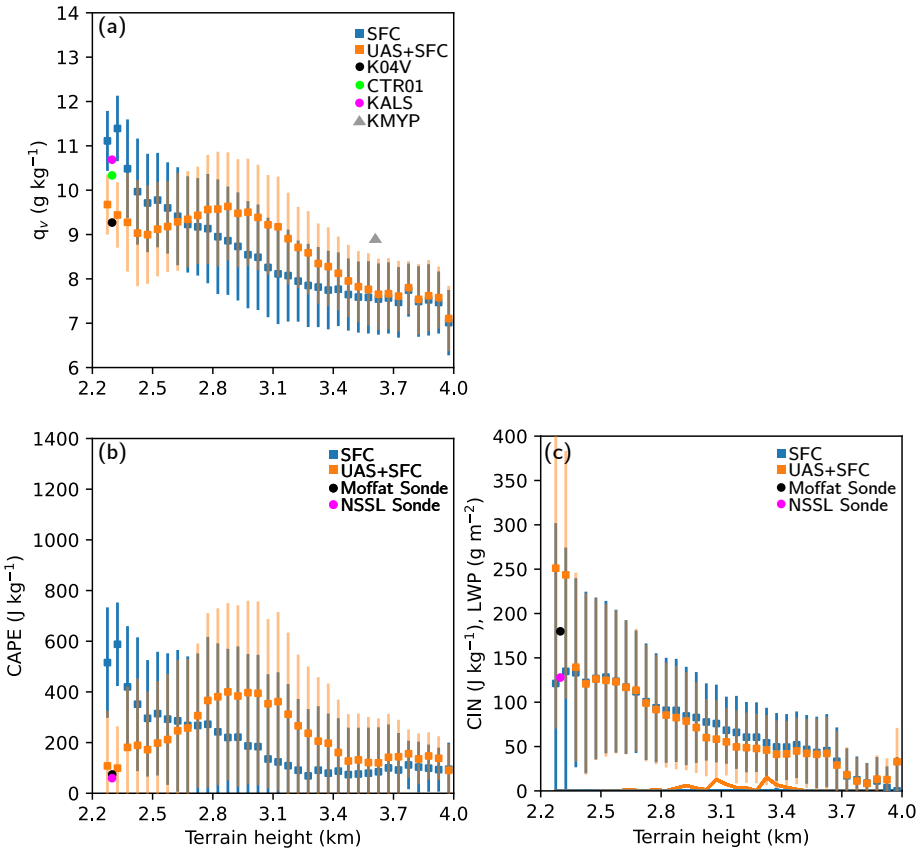

FIG. 12. Mean (filled box) and $\pm 1\sigma$ (whiskers) for each terrain height bin of (a) modeled q_v, (b) CAPE, and (c) CIN from lowest model level (approximately 10 m AGL). The mean LWP in each elevation range (solid lines) is also given in (c) for both SFC and UAS+SFC DA (SFC values are all zero). Values are accumulated from 40-member ensemble of priors valid at 1530 UTC on 15 July 2018 (CI case). Data from each prior are collected within a 130-km by 130-km region centered on the SLV and aggregated by terrain height in 50-m bins from 2300 – 4000 m MSL. Values from the SFC (blue) and UAS+SFC (orange) DA experiments are shown. The black, green, and magenta circles in (a) are surface-based values from Saguache, CSU, and Alamosa (~ 2300 m MSL). The gray triangle in (a) is from the Monarch Pass AWOS (KMYP) located about 150 km north of Saguache which falls outside of the assimilation domain. The circles in (b) and (c) are CAPE and CIN values calculated from the Moffat (black) and NSSL (magenta) soundings for parcels that originate approximately 10 m above the surface. CAPE and CIN values were calculated using MetPy (May et al. 2020).

1930 UTC. Evidence of the outflow from the west is not as clear in the independent observations from the MURC (SSW wind barb at 1930 UTC in Fig. 14); however, UAS observations from

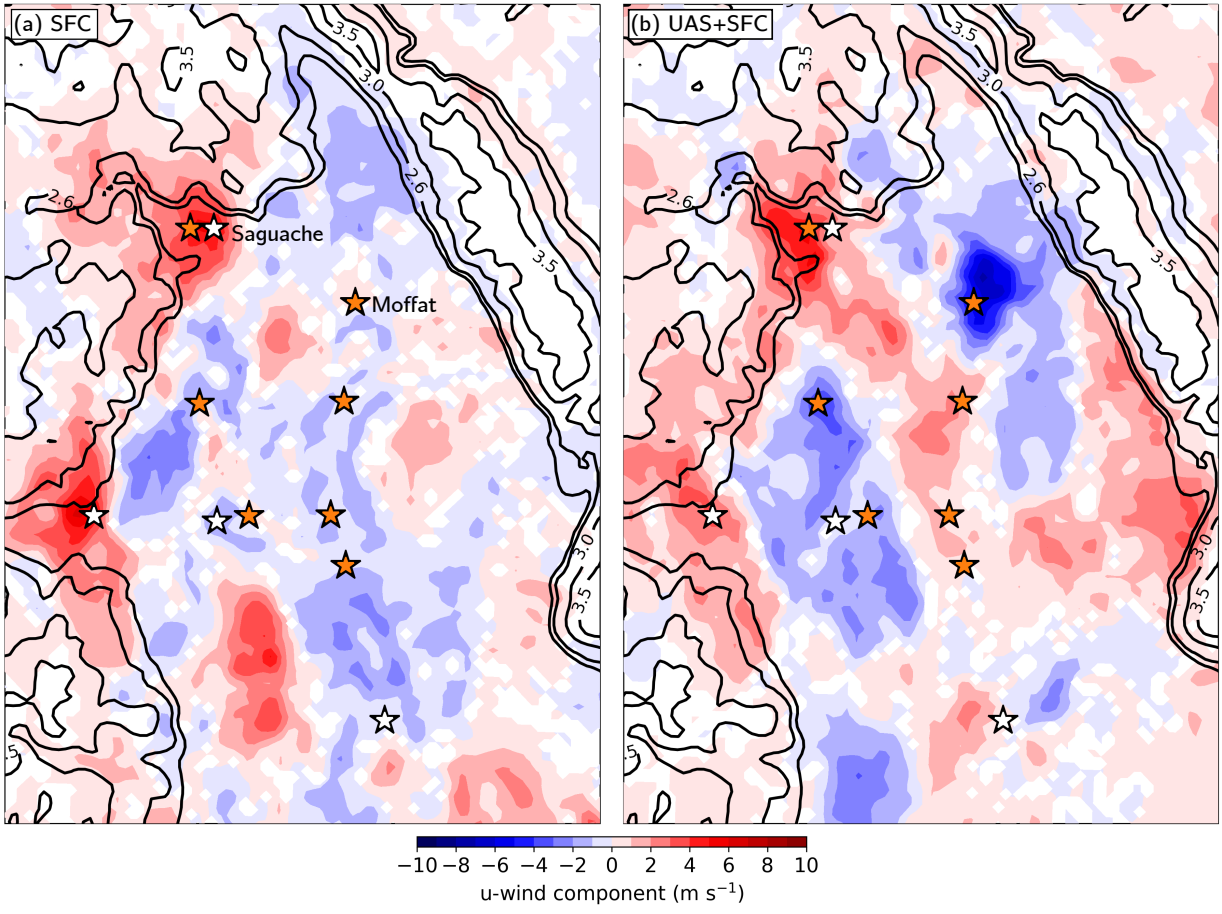

FIG. 13. Analysis increment (analysis - prior) of 10-m u-wind component at 1930 UTC on 15 July 2018 (CI case) from the (a) SFC and (b) UAS+SFC DA experiments. Values between -0.1 and 0.1 m s^{-1} are filled white. White stars denote locations of conventional surface meteorological stations used in SFC DA and orange stars denote locations of UAS profiling sites used in the UAS+SFC DA. Terrain heights are denoted by black contours in km MSL.

the Datahawk UAS on the western side of the SLV did indicate the presence of a strong westerly outflow at 1930 UTC (not shown because these measurements were well above the surface). It is noted that the lack of surface observations across the eastern half of the SLV resulted in the SFC analyses missing the outflow that impacted Moffat indicating the importance of targeted, spatially distributed profiling for obtaining observations at scales that can resolve the relevant flow features (Fig. 14b, d).

Accepted for publication in *Monthly Weather Review*. DOI 10.1175/MWR-D-22-0090.1.

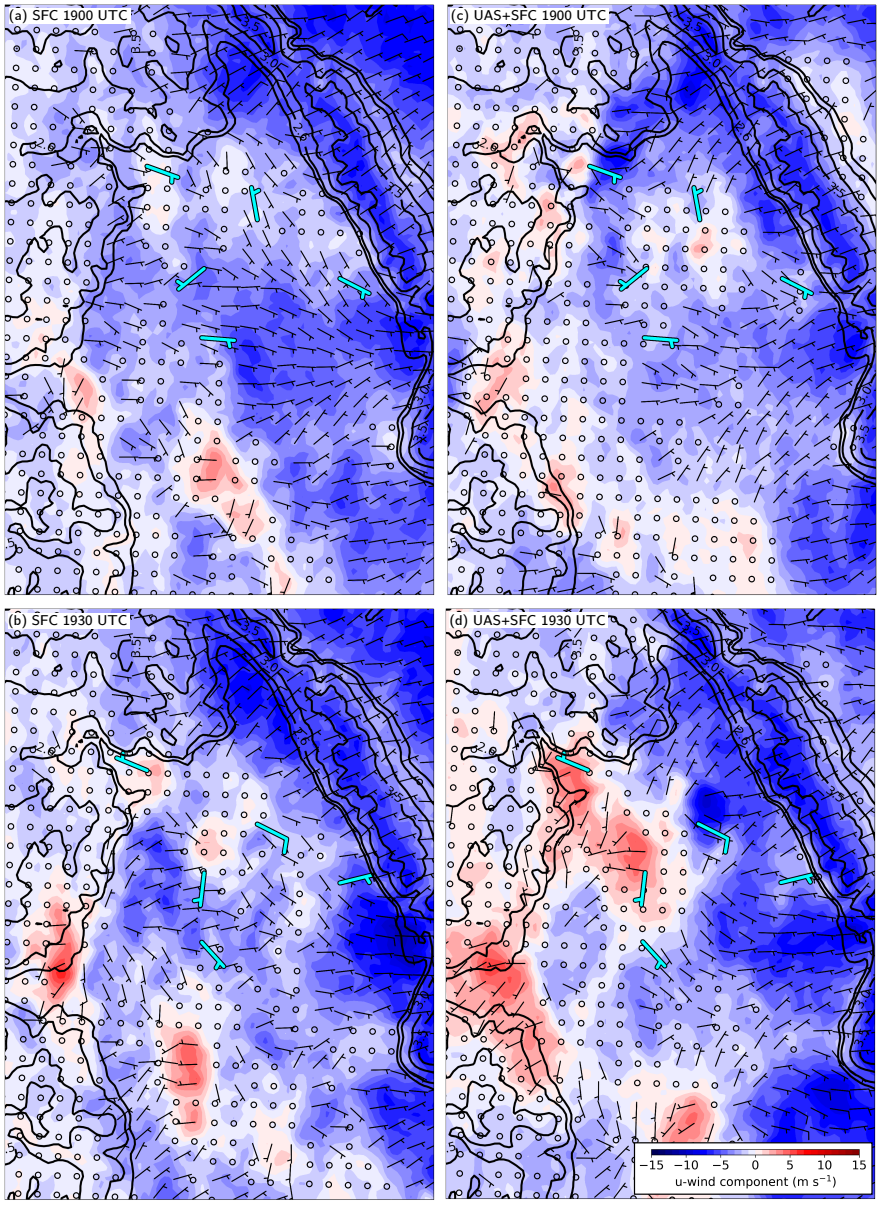

FIG. 14. Analyses of u-wind and wind barbs from the lowest model level (~13 m AGL) obtained for (a, b) SFC assimilation and (c, d) UAS+SFC assimilation valid at (a, c) 1900 and (b, d) 1930 UTC on 15 July 2018. The cyan wind barbs are from several independent observing systems (i.e., lowest return height (40 m AGL) from the Windcube Doppler lidars at Saguache and Moffat, the FMI ground station - furthest south, the CU MURC tower, and the UNL mobile mesonet - furthest east). Heights for each wind measurement vary between 2.75 and 40 m AGL as denoted in Table 3.

Accepted for publication in *Monthly Weather Review*. DOI 10.1175/MWR-D-22-0090.1.

In order to further quantify differences in the skill of analyses obtained with SFC DA versus that obtained with UAS+SFC DA, all of the ensemble mean analyses obtained with both simulations are paired in time and space with all available independent observations for the CI case. Analyses generated every 15 min between 1400 and 1945 UTC were matched in time and space with observations obtained with a range of different observing systems. The independent observations were constrained to be within 7.5 min of the model valid time. Model values were averaged across a 5 x 5 km box centered on the observation location. In addition, observations collected with profiling observing systems were vertically-averaged using a 30-m vertical sampling window centered on the model grid height. The comparisons were also confined to be within the lowest 1000 m of the atmosphere where the impacts of DA were expected to be greatest. The normalized Root Mean Squared Error (RMSE) and normalized absolute bias were computed at each model grid point for which independent observations were available. Both metrics were normalized using the standard deviation of all observed values used in the comparison (in time and height where relevant) so that the magnitudes of scores obtained for θ, q_v, and wind speed can be inter-compared. The spatial distribution of differences in these two metrics (UAS+SFC minus SFC) is shown in (Fig. 15) with negative values indicating reduced bias and reduced error. All but one (the exception being the normalized absolute bias in moisture) of the median skill scores indicate that addition of UAS DA generally improved skill across the entire domain. However, regional, variable-dependent patterns in the relative performance are evident with θ improvements associated with UAS+SFC DA being confined to the south and east of the SLV and moisture improvements being more evident in the normalized RMSE than the normalized absolute bias. The increase in the median absolute bias of analyzed moisture in the UAS+SFC DA run is caused by slightly too much drying on the eastern side of the SLV. As will be discussed below, this slight dry bias had no bearing on the predictions of CI in the center of the valley, which was accurately portrayed only in the UAS+SFC run.

5. Assessment of UAS data assimilation impacts on predictive skill

As detailed above, UAS observations had a positive impact on the skill of 4D ensemble mean analyses of temperature, moisture, and winds. In this section, the impact of the addition of UAS observations to SFC DA on the skill of free forecasts is assessed.

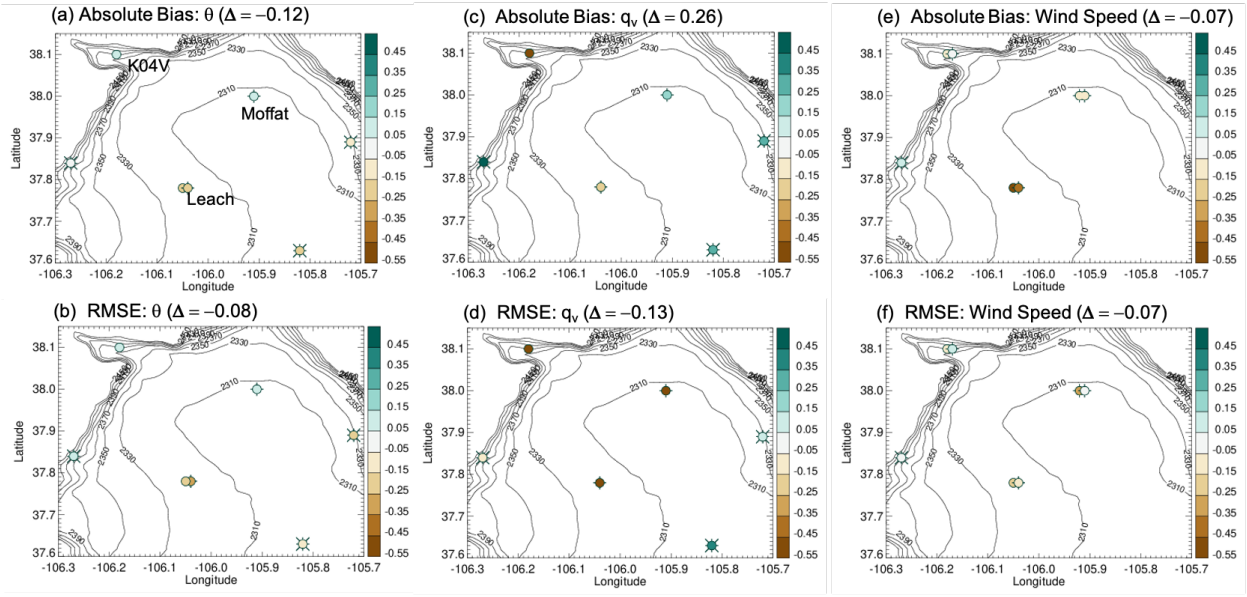

FIG. 15. Difference in normalized absolute bias and normalized RMSE for ensemble mean analyses of (a, d) θ, (b, e) q_v and (c, f) wind speed obtained for the 15 July 2018 CI case. The normalized difference is given by UAS+SFC DA minus SFC DA divided by the standard deviation in the observed values. Negative (brown) values indicate reductions in bias and RMSE afforded by UAS data assimilation. Symbols indicate the observation type: surface station (color filled circles), radiosonde profiles (color filled circles with four legs) and UAS profile data (color filled circles with eight legs). Measurements obtained at K04V (AWOS and CU Doppler Lidar), Leach Airfield (MURC and NSSL mobile sonde) and Moffat (CU Doppler Lidar and CLAMPS sondes) are slightly offset to be visible. Median differences are given in parentheses. Black contours indicate terrain height.

a. Terrain-driven flows

The finescale spatio-temporal variations and shallow nature of terrain-driven flows makes them challenging to accurately predict (Defant 1951; Orville 1964; Whiteman 2000). To assess the relative predictive value of UAS observations in addition to SFC observations for the prediction of terrain-driven flows, the ensemble mean analyses obtained at 1300 UTC for the SFC DA and UAS+SFC DA runs are used to initialize 3-h deterministic predictions. At 1300 UTC (see Fig. 6), drainage flows are still impacting both Saguache and Del Norte (low-level winds from the northwest and west, respectively) and downslope flows are influencing Moffat (easterlies flowing down the Sangre de Cristo Mountains). Just 1.5 h later at 1430 UTC (Fig. 16a, c), the observed winds just above the surface have already reversed to southeasterly at Sagauche with flow also

Accepted for publication in *Monthly Weather Review*. DOI 10.1175/MWR-D-22-0090.1.

turning southeasterly at Moffat. Also note the northeasterly wind reported at North Farm by the MURC located 20 km to the west of Moffat. These mesogamma-scale variations in the wind field are completely missed in the 1.5-h prediction obtained with SFC DA, which shows westerlies throughout the region encompassed by these three independent observations (Fig. 16a). In contrast, the UAS+SFC run captures the southeasterlies at Moffat and the shift to more southeasterly flow at the mouth of Saguache Canyon. Even the predicted area of northeasterlies directly south of Saguache Canyon nearly corresponds with the northeasterly wind observed at the MURC site (Fig. 16c).

By 1600 UTC (3 h into the free forecast), surface observations indicate that southeasterly upvalley flow was occurring across much of the northern portion of the SLV and oriented toward Saguache Canyon (Fig. 16b, d). The counterclockwise rotation of this flow is likely in response to differential heating across the SLV with flow turning up-slope toward the higher terrain to the northwest within the SLV. The biggest difference between SFC and UAS+SFC predicted surface winds at 1600 UTC is the area of northeasterlies predicted to the northeast of the Del Norte Canyon. In this region, the UAS+SFC DA resulted in a stronger northerly wind component which is more consistent with the northerly wind observed at the CSU AgMet station (labeled CSU in Fig. 1). Finally, both simulations had the same bias in the timing of the wind shift at the mouth of Del Norte Canyon where winds were still observed to be westerly until 1700 UTC. Thus, both simulations transitioned to up-canyon flow roughly 1 hour earlier than observed with the UAS+SFC simulation having stronger (and more erroneous) easterly flow than the SFC simulation. This larger error in the UAS+SFC simulation may be attributed to the fact that all of the UAS observations were far removed from this location.

In addition to overall improvements in the simulated wind field in the northern SLV, the the addition of UAS DA also improved predictions of the vertical profile of winds for the drainage flow case. At 1600 UTC, a complex wind profile was observed at Moffat that included a shallow and relatively weak southeasterly jet which transitioned to stronger northwesterly flow aloft (Fig. 17). As is evident in Fig. 16, small offsets in location of wind features can manifest as large errors when comparing observations to a single model profile. To account for potential spatio-temporal offsets between the modeled and observed evolution of the terrain-driven flows, the model data surrounding the radiosonde launch site are aggregated using a 5×5 grid centered on Moffat from

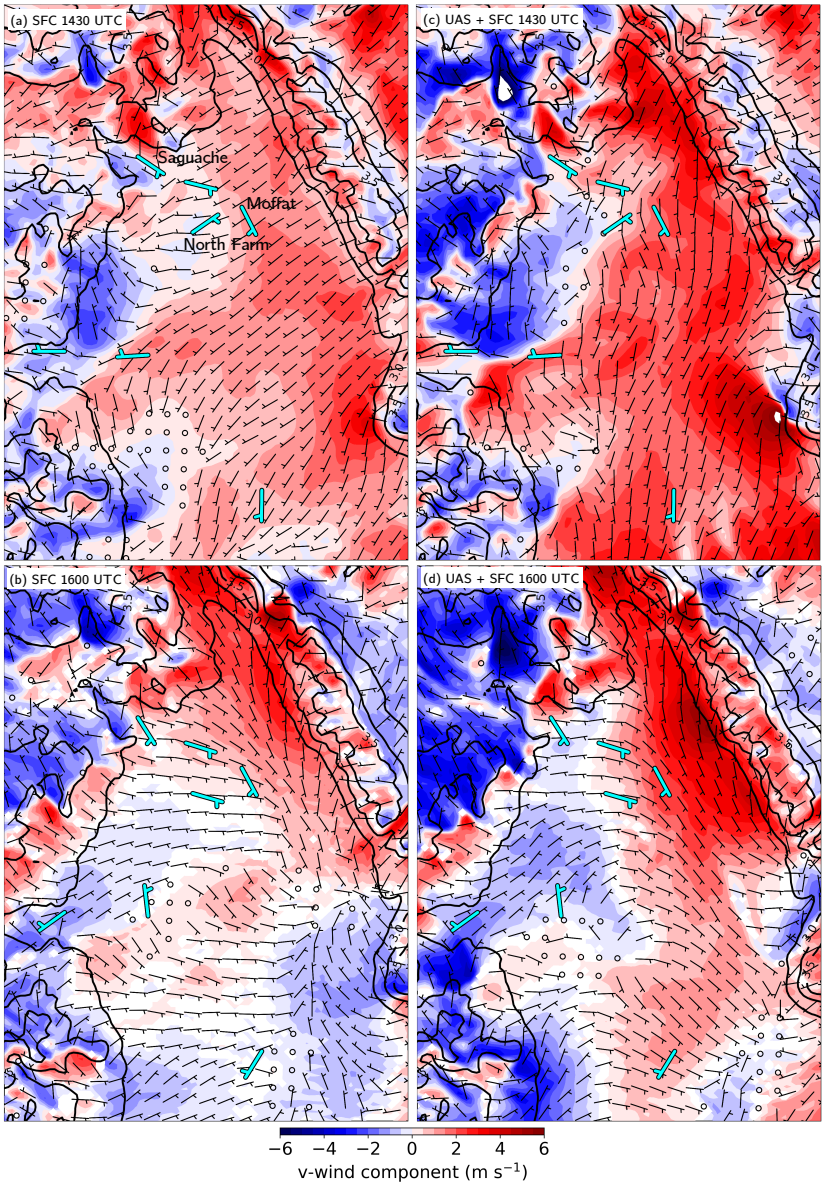

FIG. 16. Lowest model level (~13 m AGL) v-wind component (colored contours) and wind barbs (black) obtained with free forecasts initialized with 1300 UTC ensemble mean analyses obtained with (a, b) SFC DA and (c, d) UAS+SFC DA and valid at (a, c) 1430 and (b, d) 1600 UTC on 19 July 2018. Also shown are wind barbs from the lowest available level from the Windcube Doppler lidars at Saguache and Moffat, the NSSL soundings, the MURC, and the surface meteorological stations including the CSU AgMet location and stations in Del Norte and Alamosa (cyan barbs). Terrain heights are denoted by black contours in km MSL.

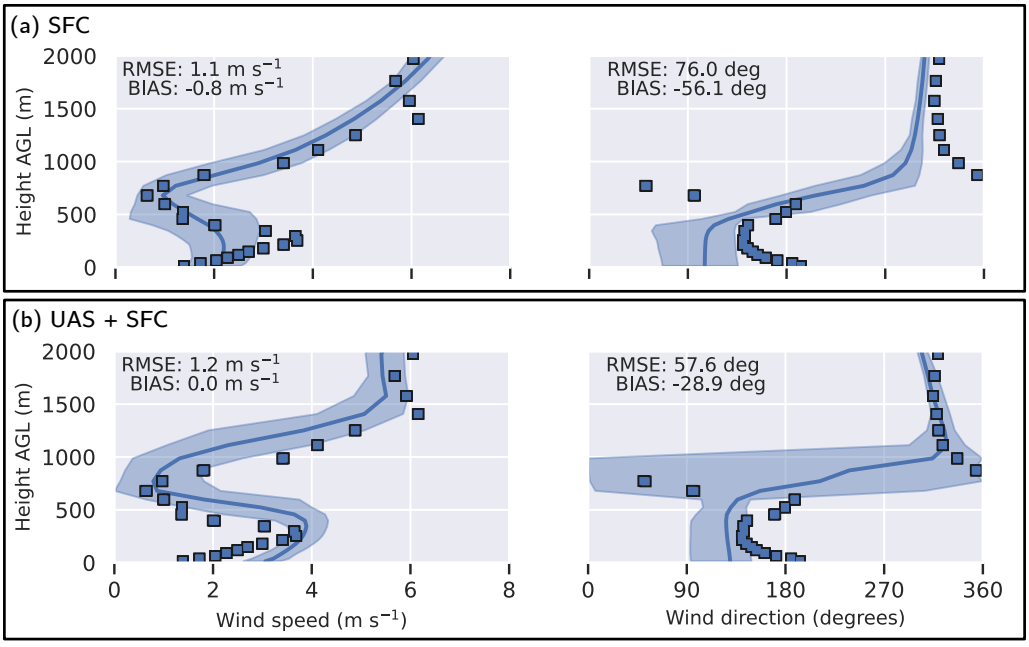

FIG. 17. Range of wind directions and wind speeds from the free forecasts initialized with the ensemble mean analysis at 1300 UTC and valid between 1530-1630 UTC on 19 July 2018 (output every 15 min) and within a 5×5 grid centered on Moffat for (a) SFC DA and (b) UAS+SFC DA. The shaded regions span all forecasted values valid within this 1-h time window and 5×5 km^2 box. The sounding data obtained from a 1600 UTC radiosonde launch at Moffat are interpolated to model levels that are indicated by the dark blue squares. RMSE and bias (model – observation) are computed using all model levels shown.

five output forecast lead times spanning the period 1530-1630 UTC. The resulting range of values provides an indication of the spatio-temporal variability in the predictions (Fig. 17).

The free forecast obtained from the UAS+SFC DA analysis at 1300 UTC captures both the direction and speed of winds in the lowest 500 m AGL better than that obtained with free forecast initialized with the SFC DA analysis (Fig. 17). While the height of the jet max is captured by both simulations, UAS+SFC DA forecast results in a much better depiction of the low-level jet maximum speed and direction with 50% reduction in the speed error and a reduction in absolute error in wind direction from 40° to 15°. While UAS+SFC DA better captures the jet maximum wind speed, it also results in a modest overestimation of the vertical extent of the low-level southeasterly flow. The cause of this biases above the jet maximum may be related to issues with the vertical mixing of momentum generated within the PBL scheme and warrants further investigation.

Accepted for publication in *Monthly Weather Review*. DOI 10.1175/MWR-D-22-0090.1.

b. Convection initiation case

Because of uncertainties inherent in the prediction of convection initiation, the performance of SFC DA versus UAS+SFC DA is evaluated using two 3-h free forecasts initialized 30 min apart. Precipitation accumulations obtained from free forecasts initialized at 1900 and 1930 UTC are compared with Stage IV precipitation analyses (Fig. 18). While neither SFC DA simulation produced appreciable precipitation within the valley (Fig. 18a, b), both UAS+SFC DA simulations resulted in large organized areas of precipitation with three hour accumulations exceeding 10 mm across the center of the SLV (Fig. 18c, d). The additional information regarding the timing and location of the outflow impacting Moffat (discussed earlier) resulted in an improved prediction of the position of the precipitation maximum in the 1930 UTC run. This finding suggests that assimilating UAS observations using a rapid update cycle can help fine tune the accuracy of predicting where and when convection initiation will occur. While the areal coverage of precipitation in the two UAS+SFC DA simulations appears to exceed that depicted by Stage IV, closer inspection of satellite and radar observations (not shown) reveals that the precipitation field expanded across most of the SLV over the next couple of hours, suggesting that the areal coverage predicted in the UAS+SFC DA simulation was fairly accurate albeit about 1 h early. It should also be noted that there is significant beam blockage of the nearest WSR-88D radars which would contribute to an underestimation of the observed rain area in the SLV (Martinaitis et al. 2020).

As mentioned above, the time evolution of winds at Moffat are critical to this particular CI prediction. Timeseries of ensemble mean winds (from both analyses and priors) are compared with Windcube Doppler lidar observations at Moffat for both SFC and UAS+SFC DA experiments (Fig. 19). The wind components have near zero mean values until after 1800 UTC. The ensemble spread of the priors (using two standard deviations) increases with time reaching over 25 m s^{-1} by 1900 UTC due to the impact of convective outflows in both simulations. The Doppler lidar measurements indicate that both wind components varied by over 20 m s^{-1} between 1930 and 2030 UTC indicating that the large uncertainty in component magnitudes was warranted.

Because there is such great variability in the analyses, free forecasts issued at slightly different times end up producing very different wind predictions. In this case, the ensemble mean analysis is not likely to be representative of the actual initial conditions and clearly demonstrates the need for ensemble prediction even for very short-range outlook periods. As discussed in Section 4,

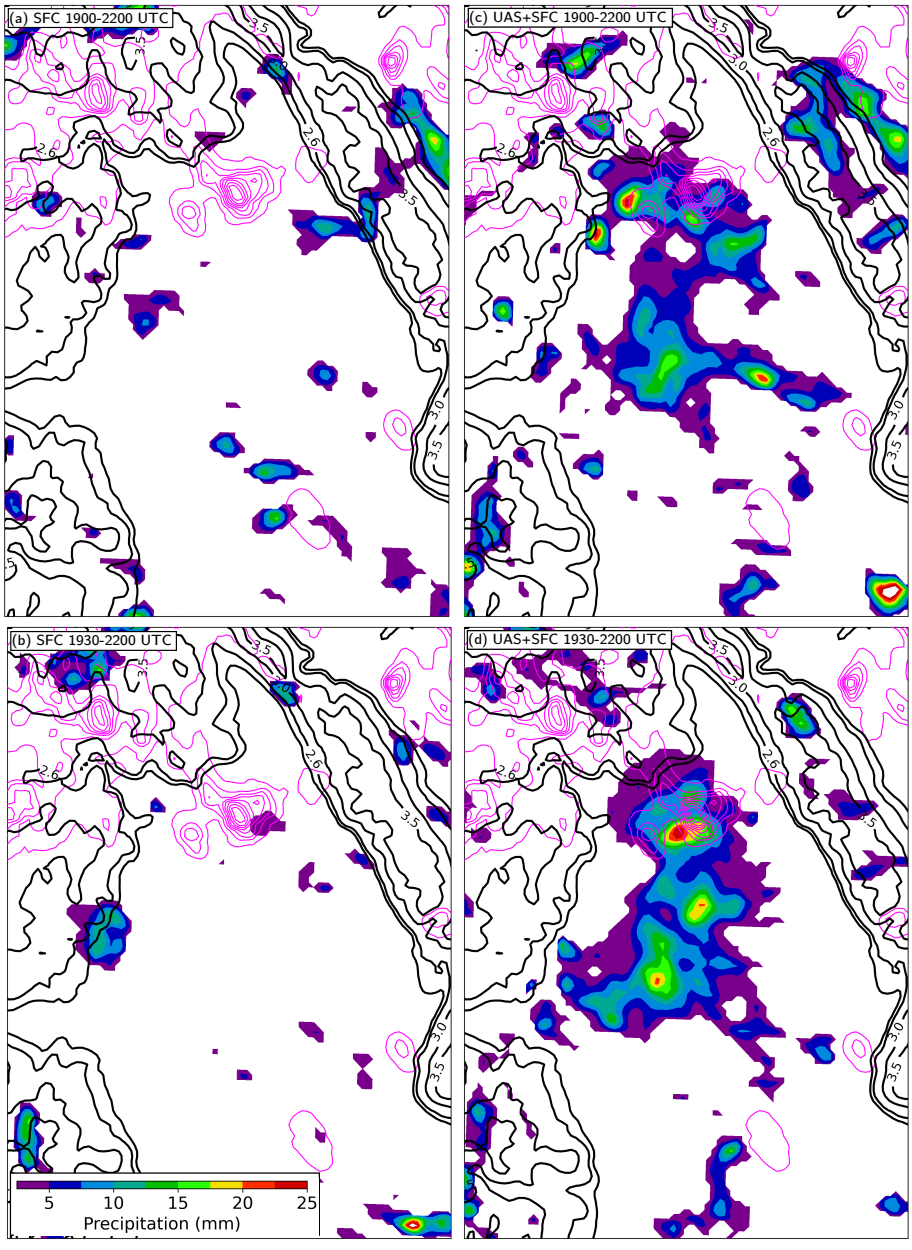

FIG. 18. Total accumulated precipitation (mm) obtained from free forecasts initialized using the ensemble mean analyses generated using (a, b) SFC DA and (c, d) UAS+SFC DA at (a, c) 1900 UTC and (b, d) 1930 UTC on 15 July 2018. The predicted accumulation is for the period ending at 2200 UTC for all simulations. The magenta contours are the Stage IV gauge-corrected 3-h (from 1900 – 2200 UTC) precipitation accumulation contoured every 2.5 mm starting from 2.5 mm. Terrain heights are denoted by black contours in km MSL.

Accepted for publication in *Monthly Weather Review*. DOI 10.1175/MWR-D-22-0090.1.

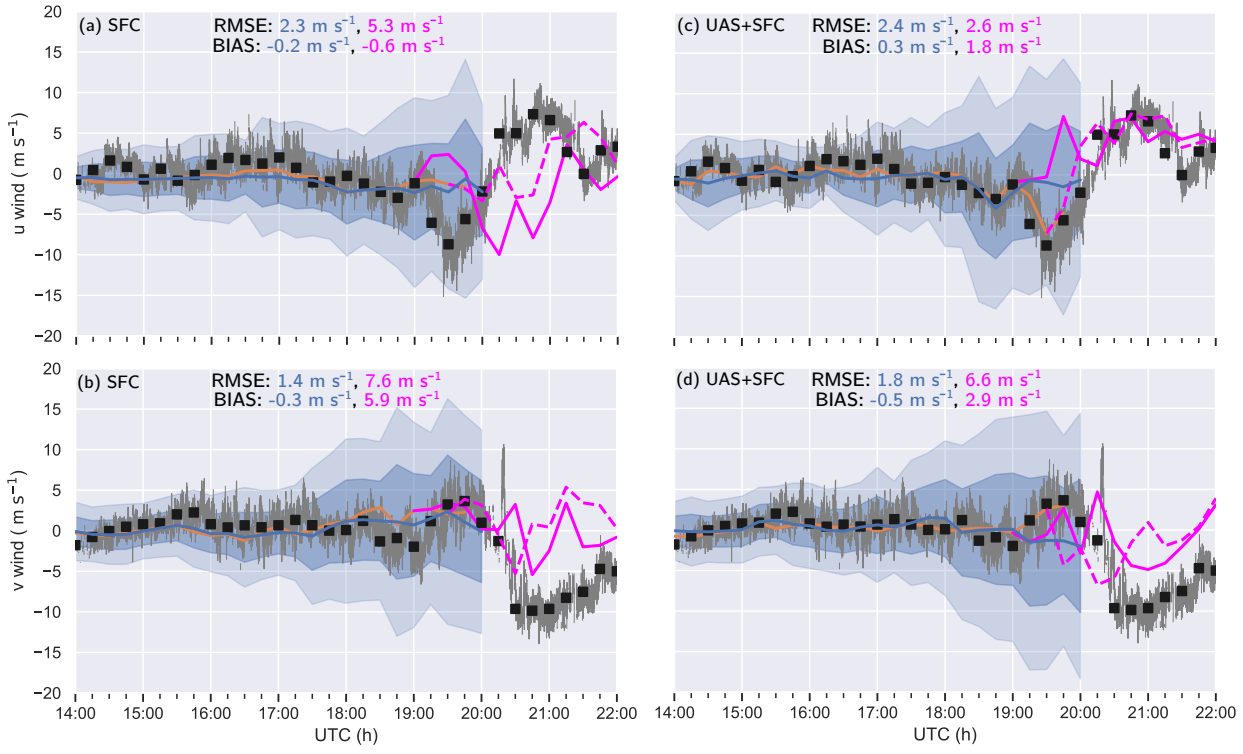

FIG. 19. Timeseries of ensemble mean of the priors (solid blue lines) and analyses (solid orange lines) for the second lowest model level (~38 m AGL) of u-wind and v-wind components at Moffat obtained from (a, b) SFC DA and (c, d) UAS+SFC DA for the 15 July 2018 convection initiation case. The dark and light blue shaded regions show 1 and 2 standard deviation(s) of the 40-member set of priors. One-second data from the lowest return height (i.e., 40-m AGL) from the Windcube Doppler lidar at Moffat is shown as the gray line with 15-minute averages denoted by the black squares. Wind components obtained from free forecasts (magenta) initialized with ensemble mean analyses at 1900 UTC (solid) and 1930 UTC (dashed) are also shown. Bias and RMSE are computed for priors (blue) and the free forecasts initialized at 1930 UTC (magenta).

a key factor in correctly simulating the location of the CI was the assimilation of observations that captured the outflow boundary that impacted Moffat. Capturing the CI location, in turn, also resulted in more accurate low-level wind predictions (Fig. 19). Note the improvements in the predicted evolution of low-level winds in the free forecasts obtained with UAS+SFC DA over that obtained with SFC DA. In fact, both SFC DA free forecasts tend to show trends in the winds that are opposite those that were observed. In particular, the u-wind RMSE of the UAS+SFC DA free forecast issued at 1930 UTC was 50% lower than that obtained with the SFC DA run (Fig. 19a, c).

Accepted for publication in *Monthly Weather Review*. DOI 10.1175/MWR-D-22-0090.1.

The improved skill in capturing the strength and timing of this wind shift is directly related to the improved analysis and short-term prediction of the precipitation and associated outflows (Fig. 18). Nonetheless, errors in the timing and strength of v-wind variations (Fig. 19b, d) remain due to small offsets in storm position and the orientation of subsequent secondary outflows. This again indicates the need for probabilistic predictions when trying to predict wind variability associated with convection at very fine scales.

Using the same method described in Section 4 and shown in Fig. 15, the skill of the free forecasts obtained for the CI case have been assessed in detail using independent truth data. A summary of this detailed assessment of the changes (UAS+SFC minus SFC) in performance of 5-h forecasts issued at 1400, 1500, and 1600 UTC and valid in 30-min increments is shown in Fig. 20. All median metric differences except absolute bias in wind speed improved with UAS+SFC DA; however, as was found with the ensemble mean analyses, these improvements were location and variable dependent. The most widespread improvements are evident in the moisture field, with particularly enhanced skill on the western and northern extents of the SLV. These reduced biases and RMSE values were critical for the evolution of convection over the foothills that produced outflows into the SLV that ultimately helped to initiate convection just north of Moffat. At the same time, absolute bias in q_v for the UAS+SFC run tended to be larger than that found in the SFC DA run in the southeast portion of the SLV. However, these increases in absolute bias in the UAS+SFC DA simulation were in areas where UAS were not flown and did not adversely impact the CI prediction.

Improvements in θ were much smaller than that found for moisture with no clear spatial pattern being evident. Improvement in the wind afforded by UAS+SFC DA simulation show up most prominently in the reduced RMSE at Moffat where the UAS DA helped to capture temporal variations associated with the passage of an outflow boundary. Note that there was also evidence of the forecasts issued at 1700 and 1800 UTC having additional skill; however, these forecasts were not included in the skill assessment since most of the independent observations were not available past 2000 UTC.

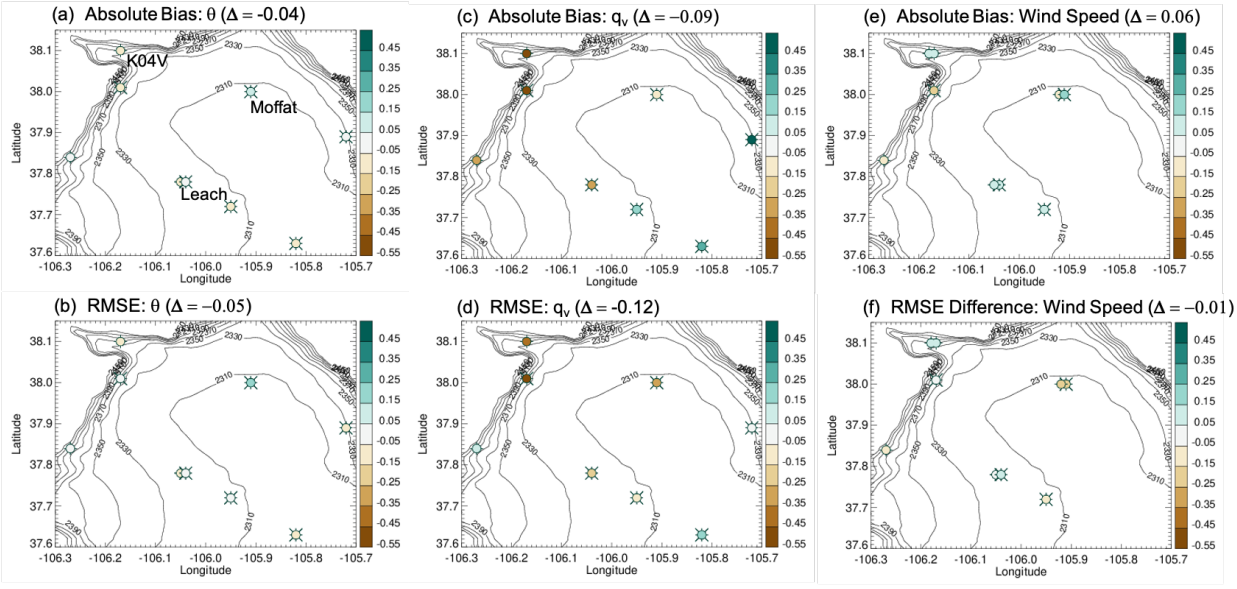

FIG. 20. As in Fig. 15, except for free forecasts of 5-h in length and issued at 1400, 1500, and 1600 UTC.

6. Summary and conclusions

The impact of assimilating UAS observations in addition to surface observations on the accuracy of analyses and the skill of short-term predictions of mesoscale flows in a data-sparse high alpine desert has been assessed using OSEs. OSEs were conducted for two cases characterized by disparate environmental conditions that were observed during the 2018 LAPSE-RATE field campaign. It was found that the assimilation of UAS observations in addition to surface observations had a positive impact on the analyses and short-term predictions of temperature, moisture, and winds in both cases and the location and intensity of convective precipitation in the CI case.

The UAS ability to perform rapid profiling and the distributed and targeted nature of the UAS observations improved the accuracy of the analyses relative to assimilating surface observations alone. The impact of assimilating UAS observations is likely to have been particularly important in the SLV due to the sparseness of conventional observations and the mesogamma-scale nature of the phenomena that were studied. It was found that the assimilation of UAS observations in addition to surface meteorological observations generally reduced biases and RMSE in the temperature, moisture, and wind fields across the SLV and improved the representation of spatial and vertical variability of these fields. Improved skill scores in both the analyses and the forecasts have been

Accepted for publication in *Monthly Weather Review*. DOI 10.1175/MWR-D-22-0090.1.

presented for the CI case. Similar improvements in overall skill were found for the terrain-driven flow case (not shown).

The two cases explored in this study offered DA challenges because they exhibited variability at space and time scales on the order of 10 km and 15 min, respectively. As discussed in (Jensen et al. 2021) and explored further in this study, the drainage flow case highlighted difficulties associated with performing DA under stably-stratified conditions in regions of complex terrain that are often characterized by shallow flows, low-level jet structures, and localized circulations. The CI case, which was characterized by complex interactions between terrain flows and convective storm outflows, demonstrated the importance of rapid cycling of the DA system in order to incorporate the latest observations needed to fine-tune the timing and location of CI. Assimilation of UAS profiles in addition to surface observations clearly improved the analyses of moisture and stability well upwind of the SLV. The assimilation of these UAS observations played a critical role in getting strong organized convection going in the foothills which ultimately produced outflows that sparked CI in the center of the SLV.

While the results presented indicate the potential value of assimilating UAS observations in addition to surface observations for improving mesogamma-scale weather prediction in observational sparse areas, a number of open areas of research remain. For example, OSEs should be performed for a range of atmospheric conditions and in areas with varying availability of conventional observations to assess where UAS observations might be expected to provide the most benefit. In addition, methods need to be developed to improve the representation of observational error covariances in the DA system (e.g., Anthes and Rieckh 2018). These observational error covariances will vary by platform type (fixed-wing versus multi-rotor) and sampling method (e.g., stepped profiling legs versus spiral profiles). Error covariances between observed variables (e.g., temperature and humidity) should also be considered in future OSEs. Finally, Observing System Simulation Experiments (OSSEs) like those conducted by (Moore 2018) are needed to assess the ideal spatio-temporal sampling patterns that could be performed by UAS across a range of environmental conditions. Additional OSSEs could also be performed to quantify the benefit of targeted UAS profiling across a range of short-term high impact weather predictions and to provide guidance for effective sampling strategies as a function of meteorological conditions.

UAS DA could also play an important role in improving finescale predictions of a number of sensible weather conditions including low-level winds, fog and low ceilings, and the freezing level which are needed across a wide range of economic sectors including agriculture, hydrology, transportation, and energy. For example, local temperature minimum and fog forecasts could be improved by continuous low-level profiling by UAS to track the evolution of winds, temperature and moisture profiles. These data could be assimilated in mesoscale models with more detailed land surface characterization for generating more accurate location specific forecast guidance. More accurate low-level wind and visibility predictions are needed to support safe and efficient expansion of UAS services that require beyond visual line of sight operations (Roseman and Argrow 2020). In fact, based on these preliminary findings, commercial UAS could actually help improve predictions of low-level winds and visibility constraints needed to support UAS Traffic Management systems by providing basic meteorological observations collected while performing their primary mission (e.g., Fleischer 2019). Ultimately, the assimilation of observations from commercial UAS coupled with those obtained with new UAS observing networks, such as the 4D mesonet discussed by Chilson et al. (2019), could result in a notable jump in the skill and reduction of uncertainty in mesoscale analyses and predictions not unlike that attributed to aircraft observations (e.g., James and Benjamin 2017; James et al. 2020).

Acknowledgments. In addition to the myriad of data collected from observing systems deployed specifically during the experiment, surface meteorological data was obtained from the Iowa Environmental Mesonet at Iowa State University and Colorado State University CoAgMET mesonet data archive. GOES and radar observations were obtained from NOAA. Authors are also appreciative of CISL's support of the Cheyenne and Casper supercomputers used to produce the simulations (Computational and Information Systems Laboratory 2019). The National Center for Atmospheric Research is sponsored by the National Science Foundation. This work was specifically supported in part by NSF Award AGS-1755088. This work was also supported, in part, by the NASA ULI program under award 80NSSC20M0162. Julie Lundquist's contribution to this paper was funded, in part, by the National Renewable Energy Laboratory, operated by Alliance for Sustainable Energy, LLC, for the U.S. Department of Energy (DOE) under Contract No. DE-AC36-08GO28308 via the Office of Energy Efficiency and Renewable Energy Wind Energy Technologies. The views expressed in the article do not necessarily represent the views of the DOE or the U.S. Government. The publisher, by accepting the article for publication, acknowledges that the U.S. Government retains a nonexclusive, paid-up, irrevocable, worldwide license to publish or reproduce the published form of this work, or allow others to do so, for U.S. Government purposes. Gijs de Boer was supported by the NOAA Physical Sciences Laboratory. Support for the LAPSE-RATE campaign was provided by the International Society for Atmospheric Research using Remotely-piloted Aircraft (ISARRA), with the US National Science Foundation (NSF AGS 1807199) and the US Department of Energy (DE-SC0018985) supporting the participation of early career scientists.

Data availability statement. Data assimilation simulations have been archived on CISL's 5-year campaign storage. UAS observations are available at https://zenodo.org/communities/lapse-rate/. The datasets used in this study are: Bailey et al. (2020); Greene et al. (2020); Jacob et al. (2020); Elston and Stachura (2020); Waugh (2020a,b,c); Houston and Erwin (2020); Islam et al. (2020); de Boer et al. (2020a); Lundquist et al. (2020); Bell et al. (2020); Bell and Klein (2020); de Boer et al. (2020b,c); David et al. (2020).

References

Anderson, J. L., 2001: An ensemble adjustment Kalman filter for data assimilation. *Monthly Weather Review*, **129 (12)**, 2884–2903, https://doi.org/10.1175/1520-0493(2001)129<2884:

AEAKFF>2.0.CO;2.

Anthes, R., and T. Rieckh, 2018: Estimating observation and model error variances using multiple data sets. *Atmospheric Measurement Techniques*, **11 (7)**, 4239–4260, https://doi.org/10.5194/amt-11-4239-2018.

Bailey, S. C. C., S. W. Smith, and M. P. Sama, 2020: University of Kentucky files from LAPSE-RATE. Zenodo, URL https://doi.org/10.5281/zenodo.3923056, https://doi.org/10.5281/zenodo.3923056.

Barbieri, L., and Coauthors, 2019: Intercomparison of small unmanned aircraft system (sUAS) measurements for atmospheric science during the LAPSE-RATE campaign. *Sensors*, **19 (9)**, 2179, https://doi.org/10.3390/s19092179, URL https://www.mdpi.com/1424-8220/19/9/2179.

Bell, T., and P. Klein, 2020: OU/NSSL CLAMPS Doppler lidar data from LAPSE-RATE. Zenodo, URL https://doi.org/10.5281/zenodo.3780623, https://doi.org/10.5281/zenodo.3780623.

Bell, T., P. Klein, and D. Turner, 2020: OU/NSSL CLAMPS microwave radiometer and surface meteorological data from LAPSE-RATE. Zenodo, URL https://doi.org/10.5281/zenodo.3780593, https://doi.org/10.5281/zenodo.3780593.

Benjamin, S. G., and Coauthors, 2016: A North American hourly assimilation and model forecast cycle: The Rapid Refresh. *Monthly Weather Review*, **144 (4)**, 1669–1694, https://doi.org/10.1175/MWR-D-15-0242.1, URL https://doi.org/10.1175/MWR-D-15-0242.1.

Cassano, J. J., 2014: Observations of atmospheric boundary layer temperature profiles with a small unmanned aerial vehicle. *Antarctic Science*, **26 (2)**, 205–213, https://doi.org/10.1017/S0954102013000539, URL https://www.cambridge.org/core/product/identifier/S0954102013000539/type/journal_article.

Chilson, P. B., and Coauthors, 2019: Moving towards a network of autonomous UAS atmospheric profiling stations for observations in the earth's lower atmosphere: The 3D mesonet concept. *Sensors*, **19 (12)**, 2720, https://doi.org/10.3390/s19122720, URL https://www.mdpi.com/1424-8220/19/12/2720.

Computational and Information Systems Laboratory, 2019: Cheyenne: Hpe/sgi ice xa system (ncar community computing). Boulder, CO: National Center for Atmospheric Research, https://doi.org/10.5065/D6RX99HX.

David, B., G. Jani, K. Osku, de Boer Gijs, and H. Anne, 2020: Atmospheric aerosol, gases and meteorological parameters measured during the LAPSE-RATE campaign - Kansas State University data sets. Zenodo, URL https://doi.org/10.5281/zenodo.3736772, https://doi.org/10.5281/zenodo.3736772.

de Boer, G., S. Borenstein, C. Dixon, and B. Argrow, 2020a: University of Colorado MURC observations from LAPSE-RATE. Zenodo, URL https://doi.org/10.5281/zenodo.3875493, https://doi.org/10.5281/zenodo.3875493.

de Boer, G., D. Lawrence, and A. Doddi, 2020b: Datahawk2 files from LAPSE-RATE. Zenodo, URL https://doi.org/10.5281/zenodo.3891620, https://doi.org/10.5281/zenodo.3891620.

de Boer, G., S. Waugh, S. Borenstein, C. Dixon, W. Shanti, A. Houston, and B. Argrow, 2020c: Measurements from mobile surface vehicles during LAPSE-RATE. *Earth System Science Data*, **submitted**.

de Boer, G., and Coauthors, 2020d: Data generated during the 2018 LAPSE-RATE campaign: An introduction and overview. *Earth System Science Data*, **2020**, 1–15, https://doi.org/10.5194/essd-2020-98, URL https://essd.copernicus.org/preprints/essd-2020-98/.

de Boer, G., and Coauthors, 2020e: Development of community, capabilities, and understanding through unmanned aircraft-based atmospheric research: The LAPSE-RATE campaign. *Bulletin of the American Meteorological Society*, **101 (5)**, E684–E699, https://doi.org/10.1175/BAMS-D-19-0050.1.

Defant, F., 1951: Local winds. *Compendium of Meteorology*, M. T.F., Ed., American Meteorological Society, Boston, MA.

Dirren, S., R. D. Torn, and G. J. Hakim, 2007: A data assimilation case study using a limited-area ensemble Kalman filter. *Monthly Weather Review*, **135 (4)**, 1455–1473, https://doi.org/10.1175/MWR3358.1, URL https://journals.ametsoc.org/mwr/article/135/4/1455/68007/A-Data-Assimilation-Case-Study-Using-a-LimitedArea.

Elston, J., and M. Stachura, 2020: Black Swift Technologies S1 unmanned aircraft system observations from LAPSE-RATE. Zenodo, URL https://doi.org/10.5281/zenodo.3861831, https://doi.org/10.5281/zenodo.3861831.

Flagg, D. D., and Coauthors, 2018: On the impact of unmanned aerial system observations on numerical weather prediction in the coastal zone. *Monthly Weather Review*, **146 (2)**, 599–622, https://doi.org/10.1175/MWR-D-17-0028.1.

Fleischer, L., 2019: Weather impacts on medical supply deliveries. *UAS weather forum*, URL https://ral.ucar.edu/sites/default/files/public/events/2019/unmanned-aerial-system-uas-weather-forum/docs/2-presentation-fleischer.pdf.

Greene, B. R., and Coauthors, 2020: University of Oklahoma CopterSonde files from LAPSE-RATE. Zenodo, URL https://doi.org/10.5281/zenodo.3737087, https://doi.org/10.5281/zenodo.3737087.

Ha, S.-Y., and C. Snyder, 2014: Influence of surface observations in mesoscale data assimilation using an ensemble Kalman filter. *Monthly Weather Review*, **142 (4)**, 1489–1508, https://doi.org/10.1175/MWR-D-13-00108.1.

Higgins, R. W., Y. Chen, and A. V. Douglas, 1999: Interannual variability of the north american warm season precipitation regime. *Journal of Climate*, **12 (3)**, 653 – 680, https://doi.org/10.1175/1520-0442(1999)012<0653:IVOTNA>2.0.CO;2.

Houston, A., and A. Erwin, 2020: University of Nebraska-Lincoln mobile mesonet files from LAPSE-RATE. Zenodo, URL https://doi.org/10.5281/zenodo.3838724, https://doi.org/10.5281/zenodo.3838724.

Houtekamer, P. L., and F. Zhang, 2016: Review of the ensemble kalman filter for atmospheric data assimilation. *Monthly Weather Review*, **144 (12)**, 4489–4532, https://doi.org/10.1175/MWR-D-15-0440.1.

Islam, A., A. Houston, A. Shankar, and C. Detweiler, 2020: University of Nebraska-Lincoln Unmanned Aerial System observations from LAPSE-RATE. Zenodo, URL https://doi.org/10.5281/zenodo.4306086, This work was partially supported by NSF IIA-1539070, IIS-1638099, and USDA-NIFA 2017-67021-25924. Limited general support for LAPSE-RATE was provided

by the US National Science Foundation (AGS 1807199)and the US Department of Energy (DE-SC0018985) in the form of travel support for early-career participants. Support for the planning and execution of the campaign was provided by the NOAA Physical Sciences Division and NOAA UAS Program., https://doi.org/10.5281/zenodo.4306086.

Jacob, J., V. Natalie, A. Avery, C. Crick, B. Hemingway, and A. Frazier, 2020: Oklahoma State University files from LAPSE-RATE: Part 1. Zenodo, URL https://doi.org/10.5281/zenodo.3700749, https://doi.org/10.5281/zenodo.3700749.

James, E. P., and S. G. Benjamin, 2017: Observation System Experiments with the hourly updating Rapid Refresh model using GSI hybrid ensemble–variational data assimilation. *Monthly Weather Review*, **145 (8)**, 2897–2918, https://doi.org/10.1175/MWR-D-16-0398.1, URL http://journals.ametsoc.org/doi/10.1175/MWR-D-16-0398.1.

James, E. P., S. G. Benjamin, and B. D. Jamison, 2020: Commercial-Aircraft-Based Observations for NWP: Global Coverage, Data Impacts, and COVID-19. *Journal of Applied Meteorology and Climatology*, **59 (11)**, 1809–1825, https://doi.org/10.1175/JAMC-D-20-0010.1, URL https://journals.ametsoc.org/view/journals/apme/59/11/JAMC-D-20-0010.1.xml.

Jensen, A. A., and Coauthors, 2021: Assimilation of a coordinated fleet of uncrewed aircraft system observations in complex terrain: Enkf system design and preliminary assessment. *Monthly Weather Review*, **in press**, https://doi.org/10.1175/MWR-D-20-0359.1.

Koch, S. E., M. Fengler, P. B. Chilson, K. L. Elmore, B. Argrow, D. L. Andra, and T. Lindley, 2018: On the Use of Unmanned Aircraft for Sampling Mesoscale Phenomena in the Preconvective Boundary Layer. *Journal of Atmospheric and Oceanic Technology*, **35 (11)**, 2265–2288, https://doi.org/10.1175/JTECH-D-18-0101.1, URL https://journals.ametsoc.org/view/journals/atot/35/11/jtech-d-18-0101.1.xml.

Leuenberger, D., A. Haefele, N. Omanovic, M. Fengler, G. Martucci, B. Calpini, O. Fuhrer, and A. Rossa, 2020: Improving high-impact numerical weather prediction with lidar and drone observations. *Bulletin of the American Meteorological Society*, **101 (7)**, E1036–E1051, https://doi.org/10.1175/BAMS-D-19-0119.1, URL https://journals.ametsoc.org/bams/article/101/7/E1036/345592/Improving-HighImpact-Numerical-Weather-Prediction.

Limpert, G. L., and A. L. Houston, 2018: Ensemble Sensitivity Analysis for Targeted Observations of Supercell Thunderstorms. *Monthly Weather Review*, **146 (6)**, 1705–1721, https://doi.org/10.1175/MWR-D-17-0029.1, URL https://journals.ametsoc.org/doi/10.1175/MWR-D-17-0029.1.

Luce, H., L. Kantha, H. Hashiguchi, and D. Lawrence, 2019: Estimation of Turbulence Parameters in the Lower Troposphere from ShUREX (2016–2017) UAV Data. *Atmosphere*, **10 (7)**, 384, https://doi.org/10.3390/atmos10070384, URL https://www.mdpi.com/2073-4433/10/7/384.

Lundquist, J. K., P. Murphy, and C. Plunkett, 2020: LAPSE-RATE ground-based Doppler lidar datasets from University of Colorado Boulder. Zenodo, URL https://doi.org/10.5281/zenodo.3804164, Funding supported by the US National Science Foundation under grant AGS-1554055., https://doi.org/10.5281/zenodo.3804164.

Martinaitis, S. M., and Coauthors, 2020: A Physically Based Multisensor Quantitative Precipitation Estimation Approach for Gap-Filling Radar Coverage. *Journal of Hydrometeorology*, **21 (7)**, 1485–1511, https://doi.org/10.1175/JHM-D-19-0264.1, URL https://journals.ametsoc.org/view/journals/hydr/21/7/jhmD190264.xml.

May, R. M., S. C. Arms, P. Marsh, E. Bruning, J. R. Leeman, K. Goebbert, J. E. Thielen, and Z. S. Bruick, 2020: Metpy: A Python package for meteorological data. Unidata, url-https://github.com/Unidata/MetPy, https://doi.org/10.5065/D6WW7G29.

Moore, A., 2018: Observing system simulation experiment studies on the use of small UAV for boundary-layer sampling. *University of Oklhoma, Master's Thesis*, 147 pp., URL https://shareok.org/handle/11244/301347.

Orville, H. D., 1964: On mountain upslope winds. *Journal of the Atmospheric Sciences*, **21 (6)**, 622–633, https://doi.org/10.1175/1520-0469(1964)021<0622:OMUW>2.0.CO;2, URL https://doi.org/10.1175/1520-0469(1964)021<0622:OMUW>2.0.CO;2.

Parrish, D. F., and J. C. Derber, 1992: The National Meteorological Center's spectral statistical-interpolation analysis system. *Monthly Weather Review*, **120 (8)**, 1747–1763, https://doi.org/10.1175/1520-0493(1992)120<1747:TNMCSS>2.0.CO;2, URL https://doi.org/10.1175/1520-0493(1992)120<1747:TNMCSS>2.0.CO;2.

Petersen, R. A., 2016: On the impact and benefits of AMDAR observations in operational forecasting—Part I: A review of the impact of automated aircraft wind and temperature reports. *Bulletin of the American Meteorological Society*, **97 (4)**, 585–602, https://doi.org/10.1175/BAMS-D-14-00055.1, URL https://journals.ametsoc.org/bams/article/97/4/585/216219/On-the-Impact-and-Benefits-of-AMDAR-Observations.

Petersen, R. A., L. Cronce, R. Mamrosh, R. Baker, and P. Pauley, 2016: On the Impact and Future Benefits of AMDAR Observations in Operational Forecasting: Part II: Water Vapor Observations. *Bulletin of the American Meteorological Society*, **97 (11)**, 2117–2133, https://doi.org/10.1175/BAMS-D-14-00211.1, URL https://journals.ametsoc.org/doi/10.1175/BAMS-D-14-00211.1.

Pinto, J. O., A. A. Jensen, P. A. Jiménez, T. Hertneky, D. Muñoz-Esparza, A. Dumont, and M. Steiner, 2021: Realtime WRF-LES simulations during 2018 LAPSE-RATE. *Earth System Science Data*, **13**, 697–711, https://doi.org/10.5194/essd-13-697-2021.

Pu, Z., H. Zhang, and J. Anderson, 2013: Ensemble Kalman filter assimilation of near-surface observations over complex terrain: comparison with 3DVAR for short-range forecasts. *Tellus A: Dynamic Meteorology and Oceanography*, **65 (1)**, 19 620, https://doi.org/10.3402/tellusa.v65i0.19620, URL https://doi.org/10.3402/tellusa.v65i0.19620.

Roseman, C. A., and B. M. Argrow, 2020: Weather hazard risk quantification for sUAS safety risk management. *Journal of Atmospheric and Oceanic Technology*, **37 (7)**, 1251–1268, https://doi.org/10.1175/JTECH-D-20-0009.1, URL https://journals.ametsoc.org/jtech/article/37/7/1251/348402/Weather-Hazard-Risk-Quantification-for-sUAS-Safety.

Skamarock, W. C., and Coauthors, 2008: A description of the Advanced Research WRF version 3. Tech. Note TN-475+STR, NCAR. URL $http://www2.mmm.ucar.edu/wrf/users/docs/arw_v3.pdf$.

Torn, R. D., and G. J. Hakim, 2008: Performance Characteristics of a Pseudo-Operational Ensemble Kalman Filter. *Monthly Weather Review*, **136 (10)**, 3947–3963, https://doi.org/10.1175/2008MWR2443.1, URL https://journals.ametsoc.org/doi/10.1175/2008MWR2443.1.

Wagner, J. S., A. Gohm, and M. W. Rotach, 2015: The impact of valley geometry on daytime thermally driven flows and vertical transport processes. *Quarterly Journal of the Royal Meteorological Society*, **141 (690)**, 1780–1794, https://doi.org/10.1002/qj.2481.

Waugh, S., 2020a: National Severe Storms Laboratory mobile mesonet data files from LAPSE-RATE. Zenodo, URL https://doi.org/10.5281/zenodo.3738175, https://doi.org/10.5281/zenodo.3738175.

Waugh, S., 2020b: National Severe Storms Laboratory Mobile Soundings during Lapse-Rate. Zenodo, URL https://doi.org/10.5281/zenodo.3720342, https://doi.org/10.5281/zenodo.3720342.

Waugh, S., 2020c: National Severe Storms Laboratory Mobile soundings during LAPSE-RATE (CLAMPS trailer). Zenodo, URL https://doi.org/10.5281/zenodo.3720444, https://doi.org/10.5281/zenodo.3720444.

Whiteman, C. D., 2000: *Mountain meteorology: fundamentals and applications*. Oxford University Press, New York.

Witte, B., R. Singler, and S. Bailey, 2017: Development of an unmanned aerial vehicle for the measurement of turbulence in the atmospheric boundary layer. *Atmosphere*, **8 (12)**, 195, https://doi.org/10.3390/atmos8100195, URL http://www.mdpi.com/2073-4433/8/10/195.